

Density Perturbations from Primordial Magnetic Fields

Bassel Farhat

Supervisors:

Prof. Robi Banerjee Dr. Pranjal Trivedi

Thesis Submitted in Partial Fulfillment of the
Requirements for the Degree of
Masters of Science
in the

Department of Physics

Faculty of Mathematics, Informatics and Natural Sciences

19.07.2021

Matrikel-Nr.: 7234183

Abstract

Primordial magnetic fields can be a significant source of density perturbations $D\rho = (\rho - \bar{\rho})/\bar{\rho}$ and baryonic heating across the recombination epoch. In this thesis, the evolution of these perturbations and the heating were studied. These fluctuations were created from an initial magnetic field inside a box and followed across different cosmological regimes via 3D magnetohydrodynamic numerical simulations. We present numerical results for simulated PMFs ranging in strength over a factor of 500 from $B_0 = [3.9 \times 10^{-4} - 0.2]\text{nG}$, and different spectral indices, showing the redshift dependencies of net heating dissipation and the evolution of density fluctuations, their strength and distribution.

Zusammenfassung

Primordiale Magnetfelder können eine signifikante Quelle von Dichtestörungen $D\rho = (\rho - \bar{\rho})/\bar{\rho}$ und baryonischer Heizung über die Rekombinationsepoke hinweg sein. In dieser Arbeit wurde die Entwicklung dieser Störungen und der Erwärmung untersucht. Diese Fluktuationen wurden aus einem anfänglichen Magnetfeld innerhalb einer Box erzeugt und über verschiedene kosmologische Regime mittels numerischer 3D-MHD Simulationen verfolgt. Wir präsentieren numerische Ergebnisse für simulierte PMFs, die in ihrer Stärke über einen Faktor von 500 von $B_0 = [3, 9 \times 10^{-4} - 0, 2] \text{nG}$ und verschiedenen Spektralindizes, welche die Abhängigkeit der Heizungsdissipation von der Rotverschiebung und die Entwicklung der Dichtefluktuationen, ihrer Stärke und Verteilung zeigen.

Dedication

To my Mother, Father, and Partner

إلى أمي، أبي و حبيبي

Acknowledgements

I would like to thank Professor Robi Banerjee for giving me the opportunity to work on this topic and for his useful critiques of my work.

Furthermore, I would also like to express my deep gratitude to Dr. Pranjal Trivedi for his patient guidance and willingness to give his time generously to explain new concepts to me.

I would also like to thank Bastian Körtgen and Urs Schäfer for their help in familiarising me with the code. I would also like to extend my thanks to everyone in our group for the friendly atmosphere and helpful discussions and input.

A big thanks to my friends for their encouragements throughout this time.

Finally, I wish to thank my parents for their love and support, without which I would not be here today.

"Somewhere, something incredible is waiting to be known."

-Carl Sagan

Contents

1	Introduction	1
2	Theory of PMF evolution	4
2.1	Primordial Magnetic Fields	4
2.2	Primordial Stochastic Magnetic Fields	4
2.3	Free Streaming Damping	5
2.4	Heating	6
2.5	Density Perturbations	7
2.6	Structure Formation	10
3	Computational Setup	12
3.1	Flash Code	12
3.2	MHD Equations	14
3.3	Photon Drag	14
3.4	Initial Conditions	16
3.5	Modifications	18
3.6	From Code to Physical Units	18
4	Numerical Results	20
4.1	Fiducial Run	20
4.1.1	Velocities	20
4.1.2	Energy Densities	23
4.1.3	Power Spectra of Magnetic and Velocity Fields	24
4.1.4	Density Perturbation	26
4.2	Simulation Results for Different Parameters	30
4.2.1	Scale-Invariant Cases	31
4.2.2	Causal Cases	38

5 Discussion	44
5.1 Numerical Comparison	44
5.2 Analytical Comparison	45
5.3 Open Questions	46
5.3.1 Alfvén Damping Scale	46
5.3.2 Different Box Sizes	47
6 Conclusion	50
Bibliography	52
Appendices	55
A Simulation Parameters	56
B Detailed Results and Tests	57
B.1 Resolution Comparison	57
B.2 Bigger Box Run	58
B.3 Causal Power Spectra	59
B.4 Null Initial Field	61
B.5 Reynolds Number	61
B.6 Dependence of initial B on k_{\max} ?	62
C Scripts Used	64

Chapter 1

Introduction

From planets and stars to the large-scale galaxies and galaxy clusters, magnetic fields are ubiquitously observed on all scales studied so far (Subramanian; 2016). Both, the Earth (Oslon; 2013) and the Sun (Brandenburg et al.; 2012; Charbonneau; 2014), display a magnetic field due to a dynamo action. The Earth's magnetic field strength is of about one Gauss. Meanwhile, the Sun displays a changing sign of dipolar magnetic field every 11 years (Hathaway and Rightmire; 2011). On the large scales, μ Gauss strength magnetic fields have been observed in high-redshift galaxies (Bernet et al.; 2008). Moreover there are some works which detect the presence of magnetic fields in the voids between the intergalactic medium (IGM). These works have provided a lower limit of 10^{-16} Gauss magnetic fields on kpc scales (Neronov and Vovk; 2010).

The origin of magnetic fields is open to more than one interpretation, whether it is a cosmological or an astrophysical phenomena. The possibility of a cosmological origin of magnetic fields is intriguing. It suggests that these cosmic magnetic fields are relics from the early universe that get amplified by the galactic dynamo process in collapsed objects (Brandenburg et al.; 2015). It would be difficult to explain how IGM field would fill the void regions through only astrophysical processes (Furlanetto and Loeb; 2001). This would be in favor of a primordial origin of the magnetic fields. These fields are also known as primordial magnetic fields (PMF). The idea of primordial magnetogenesis is attractive since it makes it easier to explain the widespread presence of magnetic fields in the universe especially the origin of the fields observed in high-redshift protogalactic condensations (Kandus et al.; 2011). However, this idea is not problem free. During early 1970s, Harrison studied this idea where he noted that this origin requires a significant amount of vorticity that is missing in the standard cosmological models (Harrison; 1973).

A complete theory of magnetogenesis is still unclear (reviewed in (Kandus et al.; 2011; Durrer Ruth; 2013; Subramanian; 2016)).

Since magnetic fields give rise to metric and fluid perturbations through the Lorentz force, PMFs are considered strongly related to the temperature and anisotropies of the cosmic microwave background (CMB) (Subramanian; 2006; Finelli et al.; 2008; Paoletti et al.; 2009; Shaw and Lewis; 2010). During recombination, the damping of magnetohydrodynamic (MHD) modes causes the magnetic fields to convert to heat due to dissipative effects (Jedamzik et al.; 1998). This heat affects electrons as well as baryons and causes two interesting effects that emerge in the CMB spectrum. The first one is caused by the additional energy in the electrons that up-scatters the CMB photons (Jedamzik et al.; 2000). The second effect is seen by a delayed recombination due to the heated electrons and that sequentially causes the change in the power spectra as well as CMB anisotropies (Sethi and Subramanian; 2005).

The evolution of PMFs changes during different cosmological epochs. In general, and as we will see later in this thesis, as the universe expands, magnetic fields strength decreases. $B(t) \propto 1/a^2(t)$ where $B(t)$ is the strength of the field at a certain time t and $a(t)$ is the scale factor of the universe at that time.

The main issues that we are trying to tackle are the following: What is the strength, evolution and distribution of density perturbations sourced by PMFs across the recombination era. In this work, we follow the evolution of 3D MHD simulations. We are able to observe the development of density perturbations, velocity fields, net heating and the different power spectra throughout different cosmological epochs.

We find three different regimes: The photon-drag dominated regime, the transition regime, and the turbulent decay regime.

Before recombination ($z > 1100$), a photon-drag dominated regime existed, where there was no heating caused by PMFs present. At times close to recombination ($600 < z < 1100$), the photon drag starts to drop significantly which allows PMFs to source fluid motions. These motions in the fluid allow dissipation of energies via a turbulent cascade, which ultimately changes the thermal history (Sethi and Subramanian; 2005). At lower redshifts ($z < 500$), the turbulent decay regime begins, where PMFs start to decay to their current time values.

Older work were able to analytically solve the evolution of net heating in the photon-drag and the decay regimes. However due to the non linear nature of the differential

equations, there wasn't an accurate analytical description of how heating and density fluctuations actually evolve in the transition regime.

The goal of this thesis is to run and analyse 3D MHD simulations of PMF with the density perturbations they produce. The first step was to check that the behavior of our runs was consistent with work previously done by Trivedi et al. (2018). In the 2018 paper, they used the Pencil code to run the MHD simulations. However, because of how the code couldn't handle shocks and density perturbations, they were restricted to sub-sonic Alfvén speeds. Whereas in our work, we found that the Flash code is more suited to capturing the physics of $\delta\rho/\rho$ and shocks from super-sonic Alfvén velocities. The second step was to explore the growth and behavior of the density perturbations as a function of the PMF parameters. Finally is to understand the physics we have simulated, the implications and the limitations of our runs.

In the upcoming sections, we will start in section (2) by describing Primordial Magnetic fields and discuss the damping scales, density fluctuations and structure formations. In section (3), we will talk about the setup we used in the runs and how we can interpret our data in physical units. Section (4) will handle the results of our work and eventually, we will discuss them in section (5).

Chapter 2

Theory of PMF evolution

As mentioned in the introduction, there are two theories for what the origin of magnetic fields in the universe could be. Here, we are studying the primordial origin of the magnetic fields using MHD simulations.

2.1 Primordial Magnetic Fields

A possible solution to the origin of magnetic fields are PMFs that are generated by magnetic seed fields that are later amplified via dynamo mechanisms (Banerjee and Jedamzik; 2004). These seed fields can be produced by multiple processes, an example is the Biermann battery within intergalactic shocks (Kulsrud et al.; 1997).

As mentioned in the introduction, PMFs evolve as $B_0 \propto 1/a^2$. However in our context, since the coordinates inside the box are comoving coordinates this evolution is no longer applied. The fields we are studying and using in our runs are stochastic magnetic fields that follow $P_M(k) = Ak^n$. In our runs, they are the only source to net heating, velocity field and the density fluctuations. Both heating and $D\rho$ are discussed in this section, we then address the connection between magnetic fields and structure formation.

2.2 Primordial Stochastic Magnetic Fields

We begin by talking about the fields used in our runs, they are randomly generated and are correlated to a power spectrum that is specified before the simulations are ran. The power spectrum used for the stochastic magnetic fields is $P_M(k) = Ak^{n_B}$, $n_B > -3$ ($n_B = n + 2$).

The rms comoving magnetic field strength used is as follows according to Trivedi et al. (2018):

$$B_f^2 = a^4 \tilde{B}_f^2 = \int \frac{d^3 k}{(2\pi)^2} P_B(k) e^{-\lambda_f^2 k^2} = \frac{A \Gamma(\frac{n_B+3}{2})}{4\pi^2 \lambda_f^{n_B+3}} \quad (2.1)$$

$\tilde{B}_f^2 \propto (1+z)^4$ is the mean square field strength of the proper coordinates. To make this equation easier to interpret, one can simply replace the filtering scale λ_f with a time depended damping scale k_d which translates to $\lambda_f = \sqrt{2}/k_d(z)$. The magnetic field can now be expressed as a function of time by replacing λ_f in eq. (2.1):

$$B^2 = \frac{A \Gamma(\frac{n_B+3}{2})}{4\pi^2} \frac{k_d^{n_B+3}(z)}{2^{(n_B+3)/2}} \quad (2.2)$$

B can now be interpreted for different power spectra. For example, a blue spectra that is defined by high values of n_B and high initial value of k. The latter translates to having the energy being initially stored at small scales. As the simulation evolves, we expect that most of the energy will shift to higher scales thus getting smaller values of k. With that in mind, we would also expect a decay in the magnetic fields. On the other hand, working with a scale-invariant spectra, i.e. $n_B = -2.9$ ($n = -0.9$) and small values of initial k: B^2 would not be as affected. This is seen in a comparison between both spectra in figure (Fig. 4.9).

This is a very simplified way to understand how B is evolving in our runs. Keeping that in mind, we can now interpret the outcome of our simulations by just knowing the initial power spectrum.

2.3 Free Streaming Damping

During the expansion of the universe, the proper length of any perturbed region increases linearly proportional to the scale factor $l \propto a$, meanwhile the mean-free-path of photons increases faster $l_{\gamma,\text{mfp}} \propto a^3$. At some time in the expansion, the photon mean-free-path will cross the linear increase, even if it is smaller initially. When this happens and these lengths get larger than the proper length, we enter what is called the free-streaming regime (Subramanian; 2016).

As seen in Jedamzik et al. (1998) and Banerjee and Jedamzik (2004), heating of the medium and the damping in the magnetic fields happens in different phases of turbulent

and viscous regimes.

At times close to recombination, and at scales smaller than the mean free path of the photons, photons apply a drag force on the baryons, caused by them freely streaming near the baryons. The force applied is $F_D = -4/3N_e\sigma_T\rho\gamma v$.

The Alfvén speed of the baryons (in light speed units) then becomes:

$$v_{bA} = \frac{a^{-2}\tilde{B}}{\sqrt{4\pi\rho_b}} = \sqrt{\frac{3}{2R}}\sqrt{\frac{\rho_b}{\rho_\gamma}} \quad (2.3)$$

Here \tilde{B} is the rms value of the magnetic field strength. ρ_B , ρ_γ , and R are given by equations 2.4. They represent the rms magnetic and photon energies densities the baryon loading time, respectively.

$$\rho_B = \frac{a^{-4}\tilde{B}^2}{8\pi} = 9.5 \times 10^{-8} \left[\frac{\tilde{B}}{1 \text{ nG}} \right] \rho_\gamma \quad (2.4a)$$

$$\rho_\gamma = 0.26 \text{ eVcm}^{-3} \left[\frac{T_0}{2.726 \text{ K}} \right]^4 (1+z)^4 \quad (2.4b)$$

$$R = \frac{3\rho_b}{4\rho_\gamma} = \frac{666}{1+z} \left[\frac{\Omega_bh^2}{0.022} \right] \left[\frac{T_0}{2.726 \text{ K}} \right]^{-4} \quad (2.4c)$$

Substituting these three equations in equation 2.3 we get the following:

$$v_{bA} = 1.5 \times 10^{-5} (1+z)^{-\frac{1}{2}} \left[\frac{\Omega_bh^2}{0.022} \right]^{-\frac{1}{2}} \left[\frac{T_0}{2.726 \text{ K}} \right]^2 \left[\frac{\tilde{B}}{1 \text{ nG}} \right] \quad (2.5)$$

2.4 Heating

In our runs, the only energy source are the magnetic fields that we create. These magnetic fields in turn can dissipate and generate kinetic energy density ρ_{kin} . This kinetic energy is produced by driving the baryons through the Lorentz force (Trivedi et al.; 2018). The kinetic energy density $\rho_{\text{kin}} = 0.5\rho_b < v_b >^2$, where ρ_b is the baryonic energy density and v_b the baryonic velocity fields.

Nonetheless, this process is not done without loss of energy. Some of the factors that cause the loss of energy are the following:

- The small scale dissipative processes, caused by both plasma effects and Coulomb interactions.
- The interactions of the baryons with the CMB photons, caused by the photon drag.

The dissipation play a very important role in the turbulent regime, as it is the reason behind the heating of the baryons. The total energy of the runs are as follow (Trivedi et al.; 2018):

$$\frac{dE_{\text{tot}}}{dt} = \frac{dE_B}{dt} + \frac{dE_{\text{kin}}}{dt} = -2\alpha E_{\text{kin}} - HE_{\text{kin}} - \frac{dE_{\text{tot}}}{dt} \quad (2.6)$$

The total energy density in the runs are only given through kinetic and magnetic energy densities $E_{\text{tot}} = E_{\text{kin}} + E_B$. To conserve the fact that we are working with comoving coordinates, the following transformations need to be taken into account:

$$E_b = a^4 \rho_B \equiv \frac{1}{2} a^4 \rho_b < v_{A,b}^2 > \quad E_{\text{kin}} = a^4 \rho_{\text{kin}} \equiv \frac{1}{2} a^4 \rho_b < v_b^2 > \quad (2.7)$$

$v_{A,b}$ in the previous equation (2.7) is the Alfvén velocity of the baryons, and v_b the velocity field of the baryons.

The photon drag term is represented in the first term on the right hand side in equation 2.6. The HE_{kin} term is added to take into consideration the cooling happening during the expansion of the universe. This term is negligible compared to the generated heating. The last term is the one causing the actual heating through the dissipation of the magnetic field.

2.5 Density Perturbations

Primordial magnetic fields are responsible for the formation of density fluctuations. In the following two sections, we will describe the density perturbations produces by PMFs and how they affect early structure formation.

To describe these density fluctuations, we start by an analytical solutions and approximation. The MHD equations after recombination in comoving coordinates are as follow (Wasserman (1978)):

$$\bar{\rho}_b \left[\frac{\partial v}{\partial t} + H(t)v + \frac{v \cdot \nabla v}{a} \right] = \frac{1}{a} \nabla p_b + \frac{(\nabla \times B) \times B}{4\pi} - \frac{1}{a} \bar{\rho}_b \nabla \Phi - \frac{4\pi}{3} \rho_\gamma n_e \sigma_T \quad (2.8)$$

$$\frac{\partial \delta_b}{\partial t} + \frac{1}{a} \nabla \cdot v = 0 \quad (2.9)$$

$$\frac{\partial a^2 B}{\partial t} = \frac{1}{a} \nabla \times [\mathbf{v}_{\text{per}} \times (a^2 B) - \eta \frac{1}{a} \nabla \times (a^2 B)] \quad (2.10)$$

$$\nabla^2 \Phi = 4\pi G a^2 \delta \rho_T = 4\pi G a^2 [\bar{\rho}_b \delta_b + \bar{\rho}_{DM} \delta_{DM}] \quad (2.11)$$

We neglect the term $v \cdot \nabla v$ in the Euler equation 2.8 and consider the density perturbations as $\rho_b = \bar{\rho}_b(1 + \delta_b)$ where ρ_b are the initial perturbations and δ_b represent the fractional perturbations. We also take into account both baryonic and dark matter components in the Poisson equation 2.11.

The equation of state used is $p_b = \rho_b c_b^2$, where $c_b^2 = (kT/\mu)$ is the sound speed and μ represents the mean molecular weight of hydrogen H ($\mu = 0.5$).

We start by considering an ideal MHD equation, this translates to $\eta = 0$, the perturbed velocity \mathbf{v}_{per} is also neglected. Removing both these factors from equation 2.10 we find that:

$$\frac{\partial(a^2 B)}{\partial t} = 0 \quad (2.12)$$

$$B = \frac{B_0(x)}{a^2} \quad (2.13)$$

Where $B_0(x)$ is a constant that is only depended on the comoving coordinates x . We now take the divergence of the Euler equation 2.9 and use both equations 2.10, 2.11 to solve it.

$$\nabla \left(\bar{\rho}_b \left[\frac{\partial v}{\partial t} + H(t)v \right] \right) = -\frac{\nabla^2 c_b^2 \rho_b}{a} + \frac{\nabla \cdot [(\nabla \times B) \times B]}{4\pi} - \frac{\bar{\rho}_b \nabla^2 \Phi}{a} - \frac{4\rho_\gamma n_e \sigma_T \nabla v}{3} \quad (2.14)$$

Substituting the equation of state and solving ∇ , while taking into account the continuity equation one finds:

$$\bar{\rho}_b \left(\nabla \left(\frac{\partial v}{\partial t} \right) - Ha \frac{\partial \delta_b}{\partial t} \right) - \frac{4a\rho_\gamma n_e \sigma_T}{3} \frac{\delta_b}{\partial t} = -\frac{c_b^2 \bar{\rho}_b \nabla^2 \delta_b}{a} + \frac{\nabla \cdot [(\nabla \times B_0) \times B_0]}{4\pi a^4} - \frac{\bar{\rho}_b \nabla^2 \Phi}{a} \quad (2.15)$$

Multiplying by the scale factor a and dividing by $\bar{\rho}_b$ one gets:

$$-\left(\frac{\partial \nabla v}{\partial t}\right) + \left[Ha + \frac{4\rho_\gamma}{3\bar{\rho}_b}n_e\sigma_T a\right]\frac{\delta_b}{\partial t} - c_b^2\nabla^2\delta_b = 4\pi Ga^2[\bar{\rho}_b\delta_b + \bar{\rho}_{DM}\delta_{DM}] + \frac{\nabla \cdot [(\nabla \times B_0) \times B_0]}{4\pi a^3\bar{\rho}_b} \quad (2.16)$$

Solving for the first term, one gets both $\partial^2\delta_b/\partial t^2$ and aH factors. Adding them the equation finally becomes:

$$\frac{\partial^2\delta_b}{\partial t^2} + \left[2H + \frac{4\rho_\gamma}{3\bar{\rho}_b}n_e\sigma_T a\right]\frac{\partial\delta_b}{\partial t} - c_b^2\nabla^2\delta_b = 4\pi Ga^2[\bar{\rho}_b\delta_b + \bar{\rho}_{DM}\delta_{DM}] + \frac{1}{a^3}S_0(x) \quad (2.17)$$

where the source term S_0 is given by:

$$S_0 = \frac{\nabla \cdot [B_0 \times (\nabla \times B_0)]}{4\pi\bar{\rho}_b(t_0)} \quad (2.18)$$

Looking into each term of this equation, we find that magnetic fields only appear in the S_0 term, this signifies that there can be fluctuations in the density term even if the initial magnetic fields are null. The terms computed from the Poisson equation also tell us that gravity grows these fluctuations. However on the other side of the equation, we find damping from the second and third terms. This damping is caused due to the expansion of the universe and radiative viscosity, respectively (Subramanian (2016)).

At recombination, we can neglect the radiative term of the equation since the damping from the expansion of the universe is far greater. Fluid pressure can also be neglected in our context. Since we are working with length scales much larger than the thermal Jeans mass.

Equation 2.17 can now be rewritten using the remaining terms as:

$$\frac{\partial^2\delta_b}{\partial t^2} = -2H\frac{\partial\delta_b}{\partial t} + 4\pi G\rho_m\delta_m + \frac{S_0(x)}{a^3} \quad (2.19)$$

$$\frac{\partial^2\delta_m}{\partial t^2} = -2H\frac{\partial\delta_m}{\partial t} + 4\pi G\rho_m\delta_m + \frac{\rho_b}{\rho_m}\frac{S_0(x)}{a^3} \quad (2.20)$$

We combine both the dark matter and baryonic terms of the Poisson equation into a matter term, i.e. $\rho_m\delta_m = \bar{\rho}_b\delta_b + \bar{\rho}_{DM}\delta_{DM}$. The solution to equation 2.20 can be computed using a Green's function method (Sethi and Subramanian; 2005). The solution is given by:

$$\delta_m(x, t) = A(x)D_1(t) + B(x)D_2(t) - D_1(t) \int_{t_i}^t dt' \frac{S(t', x)D_2(t')}{W(t')} + D_2(t) \int_{t_i}^t dt' \frac{S(t', x)D_1(t')}{W(t')} \quad (2.21)$$

Where $W(t) = D_1(t)\dot{D}_2(t) - D_2(t)\dot{D}_1(t)$ is the Wronskian and $D_1(t)$ and $D_2(t)$ are the solution of the homogeneous part of δ_m . t_i specifies the epoch of recombination. It is important to note that earlier model predicted that perturbations cannot grow before this epoch, however we find in our simulations that this is not the case. We neglect homogeneous solutions corresponding to perturbations generated by sources before recombination. Ignoring homogeneous solutions, the final solution for 2.20 is given by:

$$\delta_m(x, t) = \frac{3\Omega_b}{5\Omega_m} \left(\frac{3}{2} \left(\frac{t}{t_i} \right)^{2/3} + \left(\frac{t_i}{t} \right) - \frac{5}{2} \right) \frac{t_i^2 S_0(x)}{a^3(t_i)} \quad (2.22)$$

$$= \frac{3\Omega_b}{5\Omega_m} \left(\frac{2}{3H_0\Omega_m^{1/2}} \right)^2 S_0(x) \left(\frac{t}{t_i} \right)^{2/3} \quad (2.23)$$

Using this solution one also finds that the evolution of δ_b is given by;

$$\frac{1}{a^2} \left(a^2 \frac{\partial \delta_b}{\partial t} \right) = \frac{3}{2} H^2 \delta_m + \frac{S_0(x)}{a^3} \quad (2.24)$$

Both equations show that the fastest growing modes are evolving as $t^{2/3}$. This means that the growth of both the baryonic and dark matter component are both evolving at the same rate.

According to Subramanian (2016), by approximating S_0 from equation 2.18 to the baryonic Alfvén velocity $S_0 \sim (kv_{bA})^2$. an analytical solution for δ_m can be given by:

$$\delta_m(z) = \frac{0.7}{1+z} \left[\frac{k}{1 \text{ Mpc}^{-1}} \right]^2 \left[\frac{B}{1 \text{nG}} \right]^2 \quad (2.25)$$

The baryonic Alfvén velocity v_{bA} was earlier computed in equation 2.5.

2.6 Structure Formation

In early re-ionisation epoch, tangled magnetic fields can induce early collapse of structure in the universe. The first structure collapse happens at length scale close to the magnetic

Jeans length. The following mass dispersion equation helps explain the effect of magnetic fields on structure formation (Sethi and Subramanian; 2005):

$$\sigma^2(R, T) = \int_0^{k_J} dk k^2 P(k) D^2(k, t) W^2(kR) \quad (2.26)$$

In this equation, k is the comoving wave-vector, $D(t)$ is a dimensionless function that holds the time dependence of equation 2.24. $W(kR)$ is the window function they used, where $W(kR) = \exp(-k^2 R^2/2)$. They describe the following cases:

- For $R \geq \lambda_J$, one finds that $\sigma \propto R^{-3}$, this means that structure formation can form earlier. However the large structures are suppressed.
- For $R = \alpha \lambda_J$, where ($\alpha \sim 1$), one finds that $k \sim k_J$ and the mass dispersion is independent of B_0 . For $k \sim k_J$ one find that:

$$\sigma^2(R, t) \propto B_0^4 / k_J^2 \alpha^2 \lambda_J^6 \propto B_0^4 k_J^4 / \alpha^2 \quad (2.27)$$

And since $k_J \propto B_0^{-1}$, we find that the mass dispersion is independent of the magnetic field strength.

- In our case, we are using stochastic magnetic fields that follow $P_m = Ak^n$, where the exponent n is the spectral index. It is important to note that the values of n are restricted by the CMB anisotropies. Any values of n that are higher than $n_B \simeq -3$ ($n \simeq -1$) will over produce CMB anisotropies in the small angular scales (Subramanian and Barrow; 2002). Sethi and Subramanian (2005) found that for values of $n_B \leq -1.5$ ($n \leq 0.5$):

$$\sigma^2(R) \propto B_0^4 / k_c^{2n_B+6} R^{2n_B+10}, \quad \text{for } k_c \sim k_J \quad (2.28)$$

We find again that $\sigma^2(R) \propto B_0^4 k_J^4$ and that the mass dispersion is independent of the magnetic field strength.

Magnetic field initial strengths are not responsible of the formation for structure. However, once the radiative damping enters the free-streaming regime, the baryons no longer feel the pressure from photons and their mean free path become as large as the Hubble radius. These cause unstable motions, that in turn causes growth in the density fluctuations of baryons. These baryonic density fluctuations then affect the fluctuations of the dark matter components via gravitational interactions. The latter then collapse due to self gravity and begin structure formations (Subramanian; 2016).

Chapter 3

Computational Setup

In this section, we describe the setup of our MHD simulations. We begin by laying out the MHD equations used in the simulations. After that, we describe the initial conditions used in the runs as well as some modifications which were needed for solving the problems at hand. Finally, we show how to convert the simulations from code to physical units.

3.1 Flash Code

The Flash code is an open radiation MHD simulation code for plasma physics and astrophysics that uses a collection of unconnected legacy codes. It consists of many modules that are of great interest to our work including:

- Magneto-hydrodynamics solver
- Equation of State: Ideal gas
- Cosmology
- Gravity

The results obtained from the Flash code are also in a format that is easy to interpret. The output types range from readable log files to HDF5 files that can be used in many visualising codes (e.g. The YT project). The YT project is a python library that is used to analyse and visualise volumetric data.

Some of the capabilities of both the Flash code and the YT project are demonstrated in (Fig. 3.1). The aim of this figure is to illustrate what is happening in the code at a

certain time-step. Taking the arrays at a certain time and plotting them in such slice plots allows a better understanding behind the physics in our simulations. This figure is a small showcase of what both programs allow us to do.

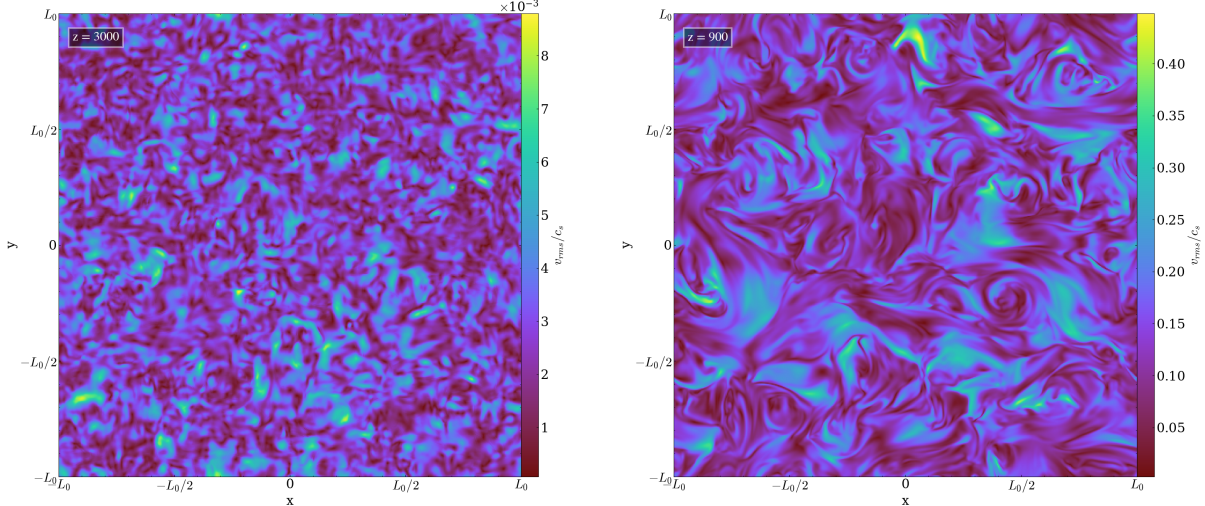


Figure 3.1: Slices representing the v_{rms}/c_s through the x-y plane at $Z = 0$ in the simulation box at two different redshifts, during the photon drag regime $z=3000$ (left panel) and near recombination $z=900$ (right panel). The fields shown are for a near scale-invariant case with $B_0 = 1$

The evolution of the velocity field at different regimes is described in figure (Fig. 3.1). The simulation ran in this figure is of high resolution ($N = 512$) with an initial magnetic field strength of $B_0 = 1$ code units $= B_0 = 3.9 \times 10^{-2}$ nG. The evolution of the velocity field is presented at two distinct redshifts. The left panel represents a time in the photon drag regime at redshift $z = 3000$. The redshift in the right panel shows the transition regime at $z = 900$.

The redshift in the right panel describes a time when the drag force lost its dominance in the box and flow was able to build up. The decrease in the amplitude of the drag force sources the Lorentz force which in turn causes the increase in the rotational component of the velocity field. This increase results in the two outcomes:

- Curls that form at high scales in the right panel
- Increase in the velocity field strength $v_{rms} = (1 - 8) \times 10^{-3}$ to $v_{rms} = (0.05 - 0.4)$

3.2 MHD Equations

As mentioned earlier, the Flash code was used to model PMFs and to simulate the behavior of density perturbations by solving the relevant MHD equations in 3D runs. We ran many simulations varying multiple different initial conditions (e.g. Initial power spectra, resolution, initial magnetic field strength, etc.). Most of our initial runs were test simulations ran at low resolutions to observe whether the simulations were describing the physics as we would expect.

After achieving convincing results, we started increasing the resolution to better explore the physics at hand. However, changing the resolution did not impact the physics in our run significantly. This is better described in convergence tests as a function of resolution in Appendix B where we show the difference of running the simulations at three different resolutions. The highest employed resolution in this work is $N = 512^3$.

The code used to run the simulations is described by the following MHD equations:

$$\frac{D \ln \rho}{Dt} = -\nabla \cdot u \quad (3.1)$$

$$\frac{\partial A}{\partial t} = u \times B - \mu j \quad (3.2)$$

$$\frac{Du}{Dt} = -\frac{\nabla p}{\rho} + \frac{j \times B}{\rho} + f_{\text{visc}} \quad (3.3)$$

Equation 3.1 represents the continuity equation of the plasma, where $D/Dt = \partial/\partial t + u \cdot \nabla$ is the convective derivative. Equation 3.2 is the induction equation of the magnetic field, where $j = \nabla \times B$ is the MHD current in the run. Equation 3.3 represents the Navier-Stokes equation, where ρ is the mass density and u is the velocity field.

3.3 Photon Drag

Photons scattering off of electrons in a free streaming regime causes damping in the magnetic field power at small scales (Jedamzik et al.; 1998). The drag coefficient in physical values is as described in equation 3.4 (Banerjee and Jedamzik; 2004).

$$\alpha = \frac{c}{R l_{\text{mfp}}} = \frac{\sigma_T N_e c}{R} = \frac{\sigma_T N_H c}{R} X_e \quad (3.4)$$

X_e is the free electron fraction (Chluba and Thomas; 2010), $N_H = 1.9 \times 10^{-7}(1+z)^3 \text{ cm}^{-3}$ the hydrogen nuclei number assuming that the helium fraction $Y_{He} = 0.24$, c the speed of light, and R the fraction of radiation density over the baryonic density $R = \rho_\gamma/\rho_b$.

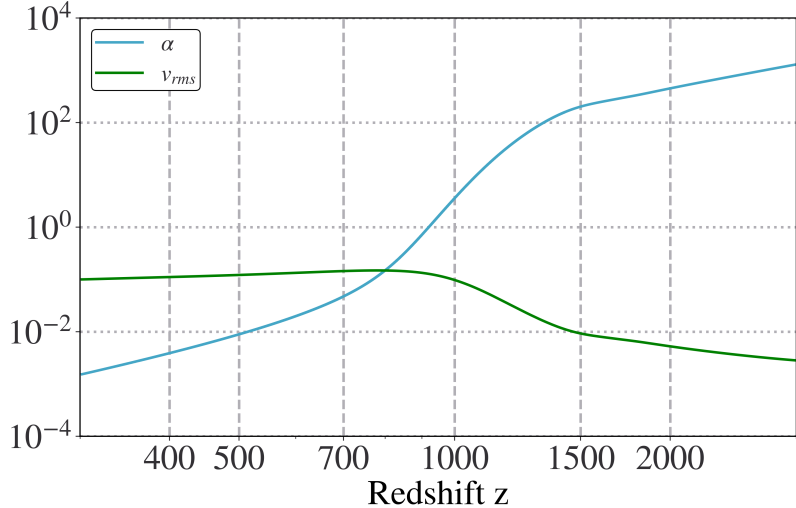


Figure 3.2: The evolution of the photon drag coefficient α (3.4) and the rms velocity field in code units for an initial $B_0 = 1$

The dominance of the drag term at high redshifts is observed in figure (Fig. 3.2). This highly viscous, drag dominated regime prevents turbulence from forming. This is the reason why v_{rms} is at its lowest value at the beginning of the run. This plot and most of the plots in this thesis only represent redshifts from $300 < z < 3000$ since earlier redshifts $3000 < z < 5000$ are affected by initial ring-in variations in the velocity and the growth of density perturbations. They are also affected by a numerical reset at $z = 4800$. Redshifts later than $z = 300$ are affected by physics that are not described in our runs such as ambipolar diffusion.

As time evolves and as the simulation reaches recombination, the drag term begins to drop significantly. This drop is caused by the formation of atoms, which in turn allows baryonic motions under the magnetic Lorentz force which ultimately lead to a turbulent flow to form. This allows the velocity field to increase in amplitude, mostly the rotational component of the velocity field. The evolution of the velocity and its components are better described in figure (Fig. 4.2).

3.4 Initial Conditions

For our initial conditions, we consider our magnetic field to be a stochastic magnetic field, where a specific power spectrum is initialized as $P_m \propto k^n$. The exponent n here represents the spectral index. To get the field mentioned, we must initialize a Gaussian random field, transform it into Fourier-space, multiply it by the selected power law, and finally, transform it back to the real space. Accordingly, we have the possibility to choose the helicity of the magnetic field that is set to 0 as initial conditions.

In this work we used two different power spectra. Both spectra are depicted in figure (Fig. 3.3). In red, the scale-invariant spectrum is presented. This power spectra is characterized by a low value of k , i.e. $k_{\text{peak}} = 2$ and by a spectral index close to -1 ($n = -0.9$). The reason why we chose this field is to show how the simulations would evolve with a spectra where energy is almost equally distributed at all length scales.

In blue, a causal power spectra is shown. The causal power spectra peak is at a higher value of k compared to the scale-invariant case $k_{\text{peak}} = 10$. The spectral indices of this spectrum were k^4 for $k < k_{\text{peak}}$ and $k^{-11/3}$ for $k > k_{\text{peak}}$. The reason behind such a power spectra is that we were restricted by any higher values then $k_{\text{peak}} = 10$ due to grid structures. We also believe that magnetogenesis would give this type of $P_M^i(k)$.

Something important to note, is that all our power spectra represent a exponential cutoff at the highest values of k . This exponential drop has been added at the end of the spectra to ensure smooth drop in the k values. Since having a sharp cut-off would not allow for any small length scale values.

To compute the power spectra in the plot, we use the built-in function `fft` in [IDL](#). The function computes the Fourier transform, we then square the results to compute the power spectra in the lower plot $P_M^i(k) = F(k)^2$.

$$F(k) = \frac{1}{N} \sum_{x=0}^{N-1} f(x) e^{-2\pi j k x / N} \quad (3.5)$$

It is important to note, that this equation was only used to perform this plot. Since we only used IDL to compute these spectra. The later power spectra in the thesis are computed and plotted using Python. The script used to compute the later power spectra can be found in Appendix C. The difference between both computation is due to how the Fourier equations are built in to each code. The differences between this plot and all the power spectra plots is a factor of $a = 1/2\pi^3$.

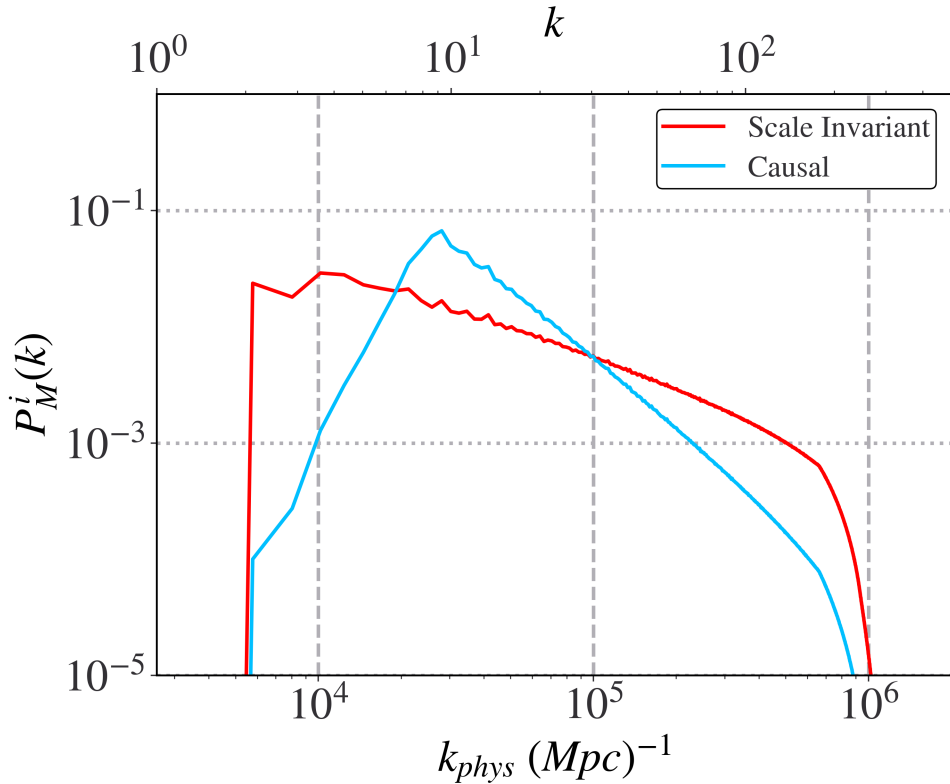


Figure 3.3: The initial power spectra used in our simulations. We show in blue the causal power spectrum and in red the near scale-invariant power spectrum. The superscript i is to inform that these are the initial spectra.

During the testing phases, we experimented with and trialled more initial conditions than we show in this thesis. Both the causal and scale-invariant spectra have been chosen as they represent a good range of the PMF origin physics we are trying to present. There were some different initial conditions that were causing some issues with the code, an example is a bluer causal spectra, i.e. a similar power spectra to the causal in this work but with a peak $k_{\text{peak}} = 60$ instead of $k_{\text{peak}} = 10$.

The simulations produced using the bluer causal power spectrum were running as expected. However, looking deeper into the data and the slices in particular, grid structures were found in the box. These structures were dominating the magnetic field through the whole simulation. They are non-physical and they forced the field to take its shape. They were mostly observed in the magnetic fields, and some in the density fluctuation fields at early redshifts. We tried multiple checks, and implemented multiple changes to the initial parameters to check if we could run such simulations since it would be interesting to be able to study the evolution of their power spectra. However, we were unable

to get a simulation running without the presence of grid structures; we chose not to use such high value of k_{peak} .

3.5 Modifications

After running multiple initial simulations, we found that the physics in our runs was not accurate. The inaccuracies we encountered were detected in grid structures at every time-steps. They were similar to the grid structures observed at high values of k_{peak} and were dominant in all the observed fields. To solve this solution, a reset to the density field in the runs to uniform values was implemented at $z=4800$. This reset was done while taking into account that the density fluctuations are reset to 0. After resetting the density, the initially purely numerical shapes get ironed out, and new random fields were produced.

We start the simulations with a null velocity field $u_{t=0} = 0$ and without the presence of a drag force. While resetting the density fluctuations at $z=4800$, we added the drag force to produce a viscous regime. This allows us to start with a turbulent initial conditions similar to what actually happened in the early universe in the pre-photon drag-dominated turbulent era.

3.6 From Code to Physical Units

The results we get by running the simulations are in a dimensionless form. The simulations ran are just a dimensionless numerical representation of the physics. It is our job to add the units needed to the output to understand what is actually happening. The simulations are running in a 3D box of code length $L = 1$ code units in all three directions. Baryon density, pressure, and sound speed are all set to one ($\rho = 1$, $p = 1$, and $c_s = 1$). This allows us to interpret the velocity of the magnetic field as $v = c_s \tilde{u}_A$ and $B = \sqrt{4\pi\rho_b} c_s \tilde{u}_A$, where \tilde{u}_A is the Alfvén velocity in code units that we set in the beginning of the run.

The strengths of the fields used vary from $B = [10^{-2} - 5]c_s$ (code units) these values translate to $B_0 = [3.9 \times 10^{-4} - 0.20] \text{ nG}$. Running simulations with magnetic fields that had a higher field strength than $B_0 = 0.20 \text{ nG}$ was causing the code to output NaNs in the outputs, which signifies that it needed modifications to be able to handle such high super-sonic values. We did not try to modify the code since we felt we had enough data to interpret and we left that task for a future project.

In order to physically interpret what is evolving in our code, there are some normalization that need to be done.

We start with the sound speed: in our code we set the sound speed to a unitary value of $c_s = 1$, this translates to $c_s = 0.17 \text{ km/s} (1+z)^{1/2}$ (Trivedi et al.; 2018) . The sound speed at recombination is $c_s = 5.7 \text{ km/s} [(1+z)/1100]^{1/2}$, this will be useful later once we compute the damping scales.

Next we compute the size of the box we are simulating. We define L_{phys} as being the box length. To interpret L_{phys} , we use Hubble time $t = H_0^{-1} = 1/(70 \text{ km/Mpc/s}) = 4.4 \times 10^{17} \text{ s}$. Using the Hubble time and the value of sound speed we get a box length:

$$L_{\text{phys}} = tc_s L_{\text{code}} = 2.42(h/0.7)^{-1} \text{ kpc} \quad (3.6)$$

Lastly we compute the value of both the physical and resolved wave-number for a resolution value of $N = 512$.

$$k_{\text{phys}} = 2\pi/L_{\text{phys}} = 2590(h/0.7) \text{ Mpc}^{-1} \quad (3.7)$$

$$k_{\text{res}} = (N/2)k_{\text{phys}} = 6.6 \times 10^5(h/0.7) \text{ Mpc}^{-1} \quad (3.8)$$

Chapter 4

Numerical Results

In this section, we will present and discuss how the physical parameters of our runs evolve by first: showing the main run of this thesis which we call the fiducial case, second: inspecting the evolution of energy density and velocities and third: discussing the power spectrum evolution of the kinetic, magnetic energies and the density perturbations. In the second part of this section, we will show the evolution of all the different simulations; i.e., how they are evolving with different parameter to get a better understanding of the physics at hand.

4.1 Fiducial Run

The fiducial run is the name of simulation with an initial magnetic field $B_0 = 3$, a resolution set to $N = 512$, and an initial scale-invariant power spectrum, where k peaks at $k_{\text{peak}} = 2$, this translates to having energy stored at all scales, but with a slightly higher amount at the peak value.

4.1.1 Velocities

The following plot (Fig. 4.1), displays how the velocities and the density perturbations evolve in the fiducial run. As previously discussed we can see the three regimes fairly easily. The dashed lines at redshift $z = 700$ and $z = 1500$ represent the separation between them.

The magnetic field in this plot is decaying through the whole run. It is the only

energy present in the beginning of the simulation and thus the only source of energy for the heating, velocity field and the density perturbations in our run.

As mentioned before, our runs begin without any drag force. The latter is later added after letting the simulation run of a small amount of time. Due to the drag force preventing turbulent flow in the first regime, the velocity field is at its lowest value.

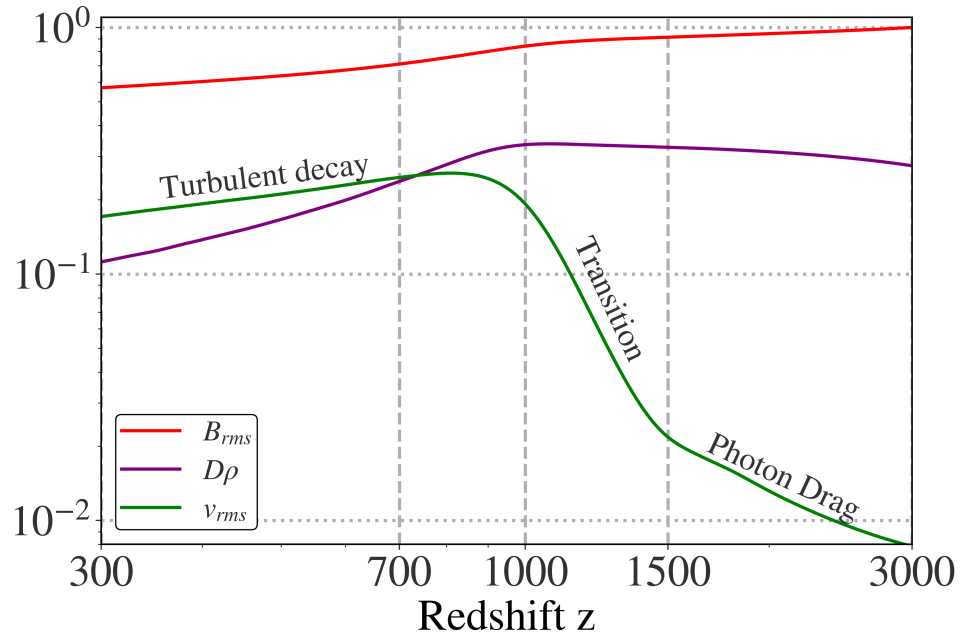


Figure 4.1: The redshift evolution of the rms value of both the velocity field of the baryons v_{rms} and the magnetic field B_{rms} , for an initial $B_0 = 3$ normalised to its value at $z = 3000$.

As the run reaches times around to recombination ($800 < z < 1500$), and as the drag force loses its suppression in the box, the velocity fields reaches its maximum. This energy gained in the baryons are lost in the magnetic field. In other words, the magnetic field is sourcing the increase in the velocity field. After reaching its maximum value $z = 800$, the velocity field starts slowly decaying.

Density perturbations are also laid out in the plot. The perturbations develop between the first and second regime. They reach a maximum at $z = 900$, the source of their increase is B_{rms} . They later decay in the turbulent decay regime, the reason behind this decay is the growth in the velocity fields. This increase causes the fields in the box to disperse hence, no more over-densities will form and the density fluctuations in the simulation drop. Density perturbations although present are not dominant.

Velocity Components The components of the velocity field are presented in figure (Fig. 4.2). The way we compute the velocity components is by using the checkpoint output files from our simulation by using the YT library. We get an array of length equal to the size of the box, in this case it is not important to know the position of the values, so we just apply ∇ of the velocity vector and take the rms value, since we would be working with N^3 values, we do this step for all the output files produced. The usual number of output files is around 22 for the low B_0 values, this means we get only 22 points to be plotted in the curve. So the next step is to apply a soft smoother to the curve. The same is done for the rotational curve, we use the following equations 4.1,4.2,4.3, store each value in an array and then take the rms of each array, and the rms of the resulting array to compute the actual rotational value of the field at that particular redshift.

$$\nabla \times v_x = \partial_y v(z) - \partial_z v(y) \quad (4.1)$$

$$\nabla \times v_y = \partial_z v(x) - \partial_x v(z) \quad (4.2)$$

$$\nabla \times v_z = \partial_x v(y) - \partial_y v(x) \quad (4.3)$$

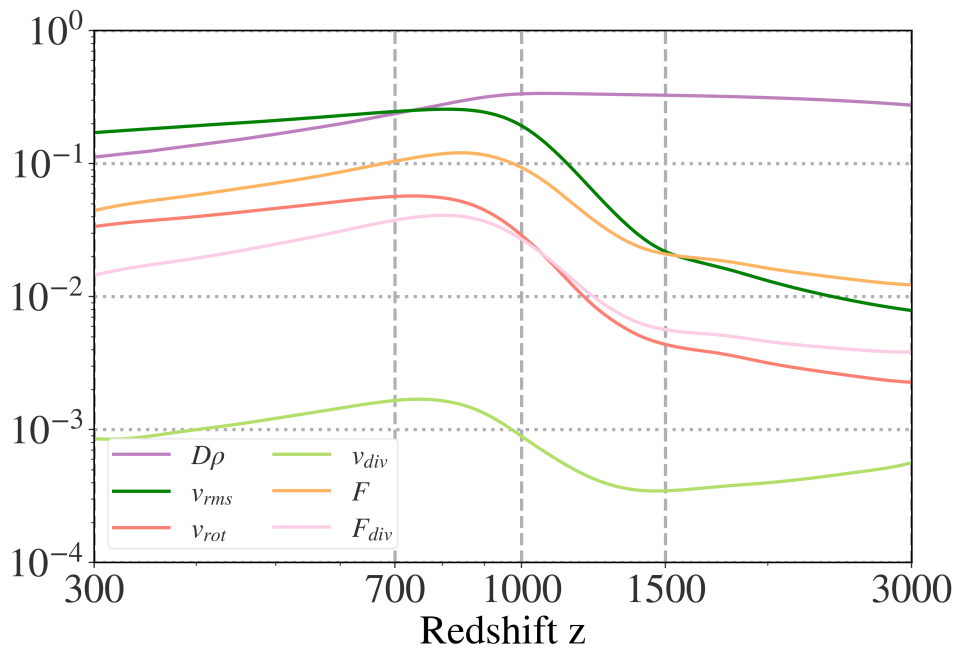


Figure 4.2: The redshift evolution of the rms value of the components of the u_{rms} and the magnetic field B_{rms} , normalised to its value at 3000, for an initial $B_0 = 3$.

The Lorentz force (purple) is also computed in the same way: we take the magnetic

field values as well as the velocity field and just apply $v \times B$. To get the divergence we just apply the ∇ to the previous equation.

Looking into the plot, the rotation component of the velocity is clearly dominant, the reason behind that is the source of the velocity field. As mentioned earlier, the magnetic field is sourcing the velocity field, thus the force applied on the field is the Lorentz force, this causes the field to rotate. The divergence in the velocity field is weak compared to the rotational component.

The development of the density fluctuation is causing the drop between redshift $z = 3000 - 1500$ in the linear velocities. However, later in the run and due to the jump in the velocity field their effect becomes negligible.

The divergence of the Lorentz force is also presented in this plot as the red curve. The ratio of Lorentz force to its divergence remains constant through the simulation. Earlier in section 2, we computed the density fluctuations, and their dependence on the divergence of the Lorentz force in equation 2.23.

The first two terms of the solution are constants, S_0 here is the divergence of the Lorentz force divided by a constant, and t is the time. This solution shows that the density fluctuations and the divergence of the Lorentz force are related by a time dependency.

4.1.2 Energy Densities

Next, we present the energy densities plot in figure (Fig. 4.3). The plot shows how the different energies evolve in the runs. We found this figure to contain all the needed physics to accurately explain what is happening in the runs.

In blue, we see the rate of change of the magnetic energy $dE_M/d\ln z$. The rate of change of the kinetic energy $dE_K/d\ln z$ is seen in two different curve (in purple and yellow), taking into account whether an increase or decrease in the kinetic energy. The total energy change $dE_T/d\ln z = d(E_K + E_M)/d\ln z$ is also seen in orange. The green curve shows us the drag force, this is computed using $2\tilde{\alpha}E_K$. Finally we can see the net heating (in red), which is the difference between the rate of change of the total energy and the drag force (2.6). Since we are working with comoving coordinates there is no need for us to add the heating due to the expansion (HE_K term).

The different regimes are easily identified in figure (Fig. 4.3). At early times in the photon-drag dominated regime, the net heating is at its lowest values. The photon

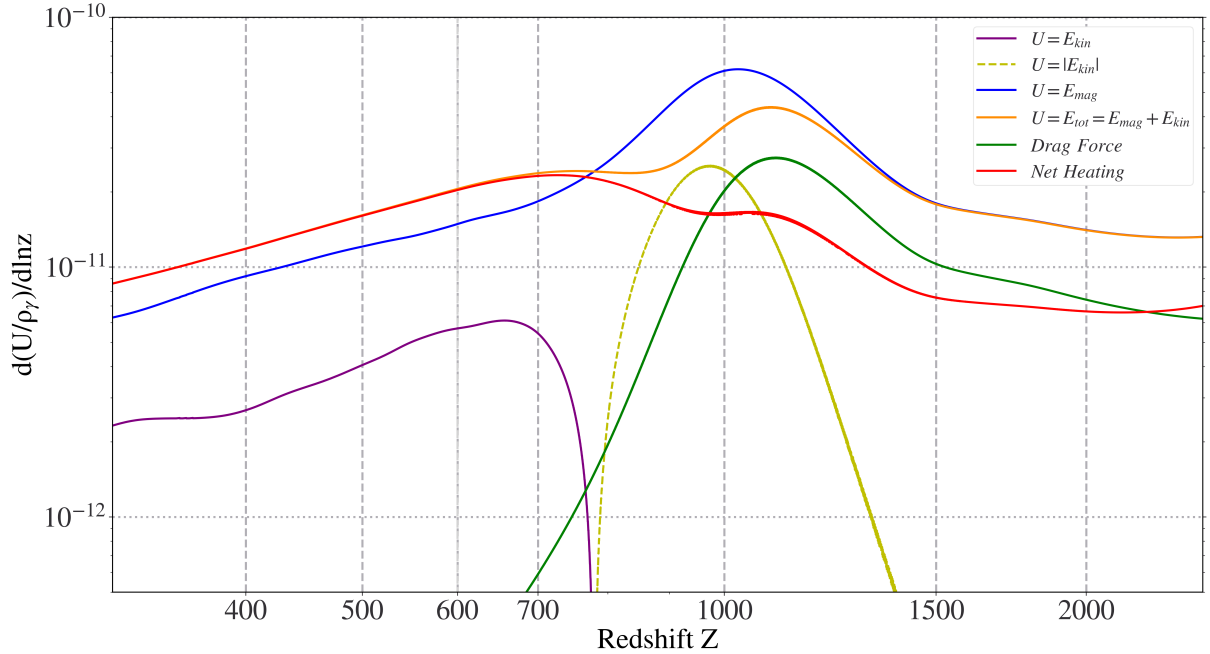


Figure 4.3: Energy density dissipation rates and net heating rate for the simulation run of near scale-invariant fiducial case power spectrum $B_0 = 3$, normalized to the energy density of radiation

drag prevents energy loss in the magnetic energy. This remains the case until we reach the transition regime at redshift $z = 1500$. In this regime, the drag begins to decay and this allows a turbulent flow to form which in turn allows the transfer of energy from the magnetic energy into kinetic energy in the baryons, as seen in figure (Fig. 4.1). Another effect caused by the decay of the drag force, is the rise of the net heating in this regime. The net heating keeps gaining amplitude in this regime. As the simulation enters the last regime, known as the turbulent decay regime the net heating reaches its maximum and starts to decay slowly.

4.1.3 Power Spectra of Magnetic and Velocity Fields

The following figure (Fig. 4.4) shows the evolution of the magnetic power spectrum (upper panel) for different redshifts for the fiducial scale-invariant initial conditions. Note, that these spectra have a $2\pi^3$ factor when comparing them to the initial magnetic fields.

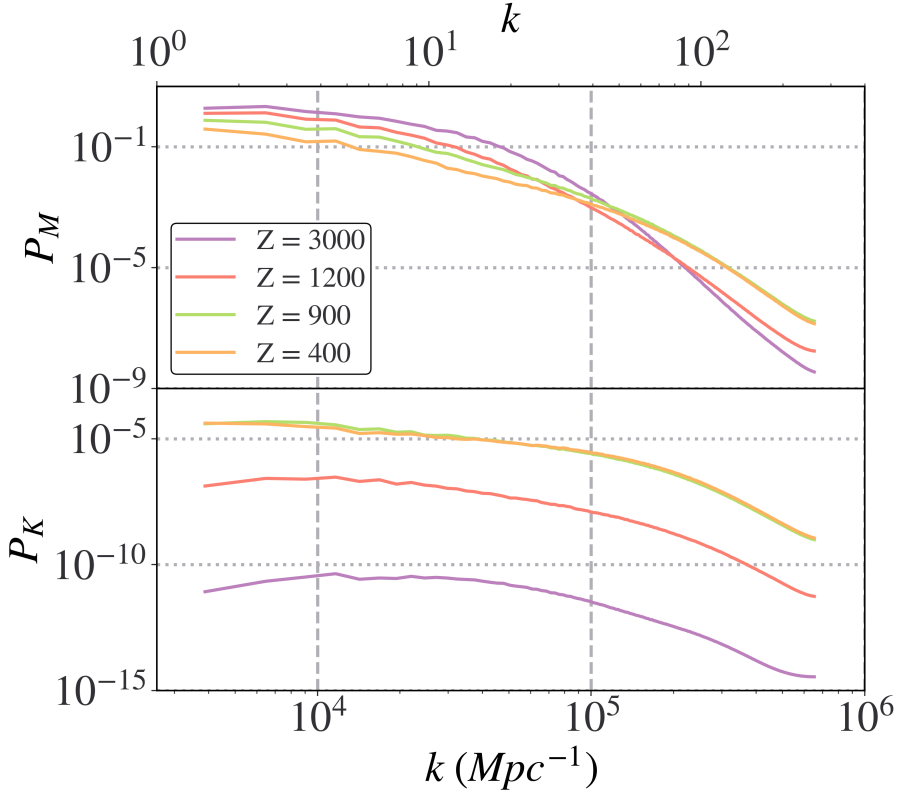


Figure 4.4: Evolution of the magnetic (solid lines) and kinetic (dashed lines) power spectra for the fiducial scale-invariant initial conditions

The redshifts in the plot are chosen to represent different times in the runs. The first one at $z = 3000$ to represent the photon drag regime, also it is at time where the initial numerical noise from the ring-in phase are no longer present and we are observing the actual physics of our run. Redshifts $z = 1200$ and $z = 900$ are in the transition regime, the former represent the beginning of the phase, and the latter to represent when the velocity field have reached the maximum during the runs. Lastly redshift $z = 400$ at the end of the simulation in the third regime where the decay has been going for some time.

Most of the energy is stored in the larger scales within the box. The decay of the magnetic field in the box can be seen by the loss of power in the lowest k values. However, the run shows a higher increase in the power stored at small scales as the simulation reaches lower redshifts.

Turbulent evolution is represented in the power spectra. Due to turbulence evolving, the cascade of energy from large to small length scales reshapes the general power spectra into a power law. This is seen at low k , where the spectra falls slightly and rises a bit

comparing the yellow and green curves.

The evolution of the kinetic field power spectra is presented in the lower panel of (Fig. 4.4). At early redshifts, the initial values of the kinetic power spectrum are very small compared to the magnetic power spectra. This is due to the weak initial velocity field. As soon as the simulation enters the transition regime, the drag force loses its suppression on the kinetic energy, this translates into a jump in the kinetic energy power spectra. The increase in energy continues until redshift $z = 900$, the maximum in the kinetic energy, as seen in (Fig. 4.1). At the end of the simulation, the kinetic energy power spectra is very similar to its earlier shape, this is due to the energy just turbulently decaying slowly in the run.

4.1.4 Density Perturbation

In this section we present and study the density fluctuations. We begin by showing their probability density function (PDF), and study their distribution by studying the kurtosis and skewness. We then show the power spectra of these perturbations at different epochs. Lastly we show heat maps comparing them to the initial magnetic field strengths at different time-steps.

Probability Distribution Function To get a better idea of how the density perturbations are evolving in our runs, the right panel of (Fig. 4.11)) represents the kernel density estimate of the fluctuations in the box. This plot is made by taking the value of the density perturbations for each point in the box, then making a histogram with these values. A probability distribution function (PDF) is then computed from the histogram. This process was also used to make the PDF of the magnetic field in the left panel of the plot.

The redshift values are the same redshifts as for the power spectra in the earlier section. Since they are the most optimal and represent the most physics at notable times during our simulations.

The under-densities of the box are more present, since a bigger portion of the curve is in the negative side of the plot. A study of the data also confirmed that we are not working with a normal distribution, since the kurtosis and skewness test of the plot both shows positive values for all the different redshift in the plot.

Comparing to (Fig. 4.1), the growth of the density perturbations are also seen

between the first two curves. In the earlier plot, we saw that the perturbation reach a maximum in the second phase. Both the red and green curve denote the second phase in this plot. Using the full width at half maximum (FWHM) of the curves, it is clear that these curves present the highest values. The last curve (orange) shows they decay in the last regime as the fluctuations reach their minimum.

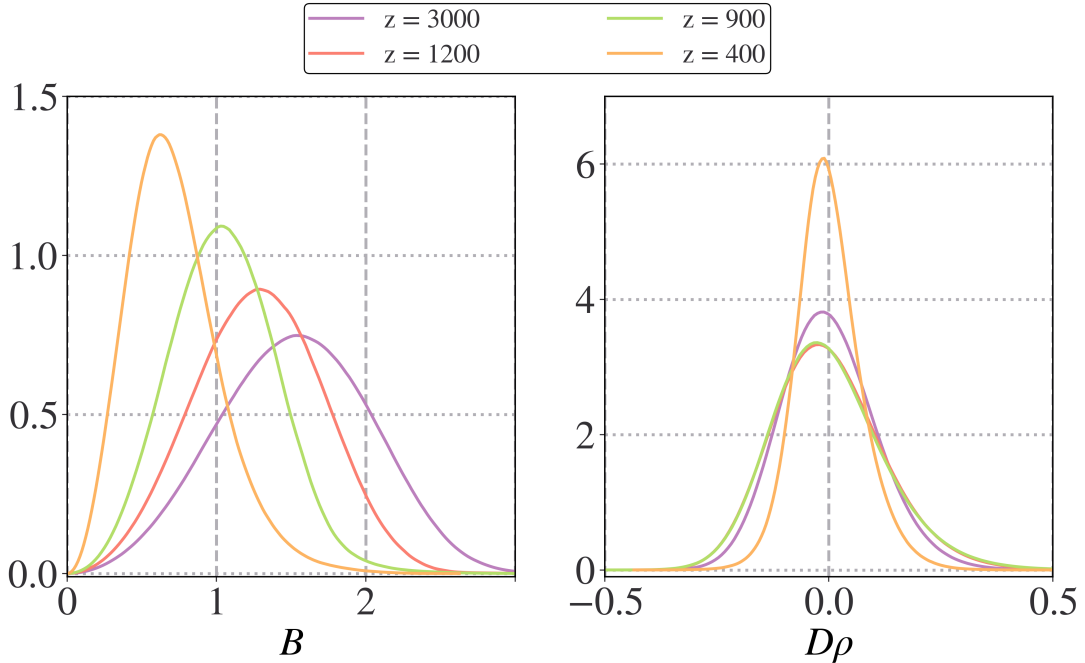


Figure 4.5: The evolution of the PDF curves of the density perturbation for different redshifts at different regimes for the fiducial case with initial $B_0 = 3$

The left panel of (Fig. 4.5) represents a PDF of the evolution of the magnetic field throughout the run. The decay of the magnetic field is represented by the decrease of the x values in (Fig. 4.5). This is what we predicted in (Chp. 2) using equation 2.2: The B field decays in the box during the simulation. Comparing the evolution of the PDF from this plot to (Fig. 4.1), also confirms the expected decay. The increase in the y axis for lower redshifts, represents a smaller range of B in the run, this translates to more points sharing similar values of B.

Kurtosis and Skewness The study of the kurtosis and skewness is a test to better interpret the distribution of our data. In our normalisation the kurtosis and skewness are equal to 0 when the distribution is a Gaussian.

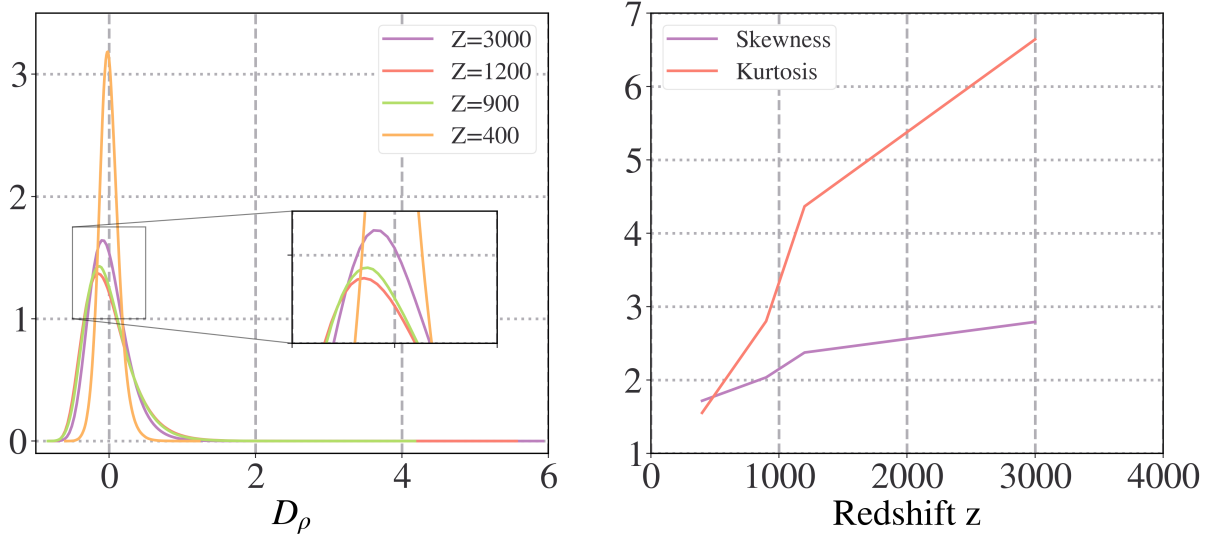


Figure 4.6: KDE plots of the density fluctuations with their respective skewness and kurtosis evolution for the scale-invariant run.

Kurtosis describes the tailness of the distribution, meanwhile the skewness describes the asymmetry of the distribution.

The kurtosis at high redshift shows a huge value, with a high value of skewness. The positive values of both factors mean that the distribution is skewed to the right, and is stretched in the y direction. As the redshift drops, both values also drop significantly. This is seen as the distribution becomes less and less skewed to the right. At the final redshift $z = 400$, the distribution has very small values of both kurtosis and skewness and almost represents a Gaussian.

Power Spectra The density fluctuation power spectra is presented in (Fig. 4.7). A Savgol filter had to be applied for this plot to smoothen the curves. The polynomial order of the filter was set to $p = 1$ and the window length $l_w = 9$. We chose these values because the presented more linear curves while keeping the shape of the power spectra. The plot describes the increase of the density perturbation between the photon drag regime and the transition regime by an increase in power value between the purple and the red curve at low values of k .

The later part of curve in both the photon drag regime and the beginning transition regime are similar. When the box reaches redshift $z = 900$, which is when the density perturbations peak, we see that the power spectra at the high wave numbers increases in

value. This indicates energy transfer to smaller length scales, which causes the density perturbations at the smallest length scales to peak at $z = 900$. The last curve shows the decay of the density fluctuations at all k scales.

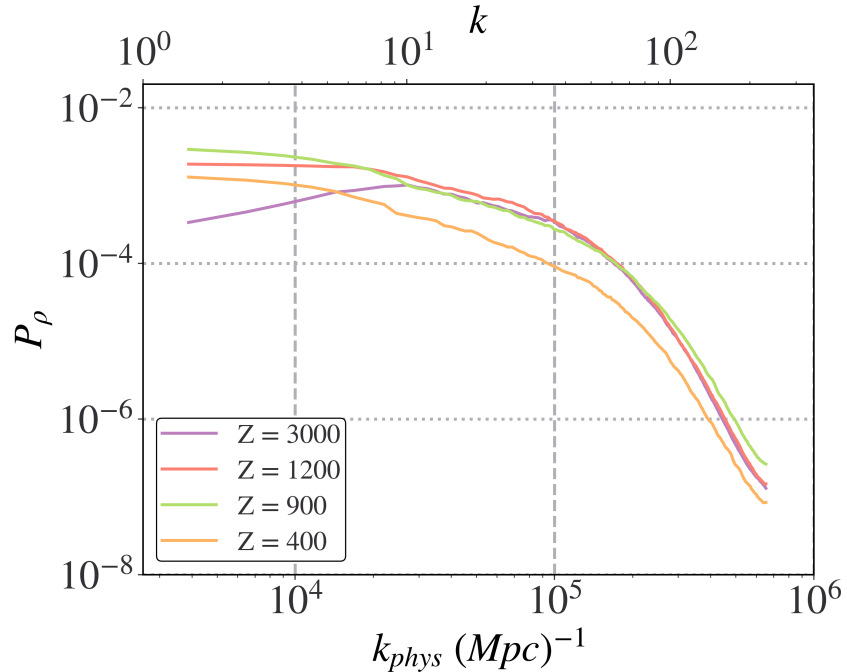


Figure 4.7: Evolution of the power spectra of the density fluctuations for the fiducial scale-invariant initial conditions

Heat Maps Looking at the data in a heat map format confirms our observations from the earlier plots. Figure (Fig. 4.8) confirms the evolution of both the magnetic field and the density fluctuations.

The redshifts of the heat maps are what we chose for the power spectra, since they represent the each epoch in the simulation. The magnetic field evolution confirms the decay happening through the simulation in each regime. The density fluctuations is also in agreement with the curve of the density fluctuations in figure (Fig. 4.1). That is presented by monotonic increase between the first two regimes, the decay happening at $z = 900$ and finally the minimum reached at the end of the simulation.

The heat maps are also accompanied with a distribution for both curves, this makes reading the data easier. Especially when searching for over and under densities. In this case the under-densities are more predominant, this confirms the results seen in the PDFs in figure (Fig. 4.11). At the beginning they are a bit more available. They grow and are

mostly observed at redshift $z = 1200$ which is when the peak of the density perturbations occur and become almost non existing at the end of the simulation.

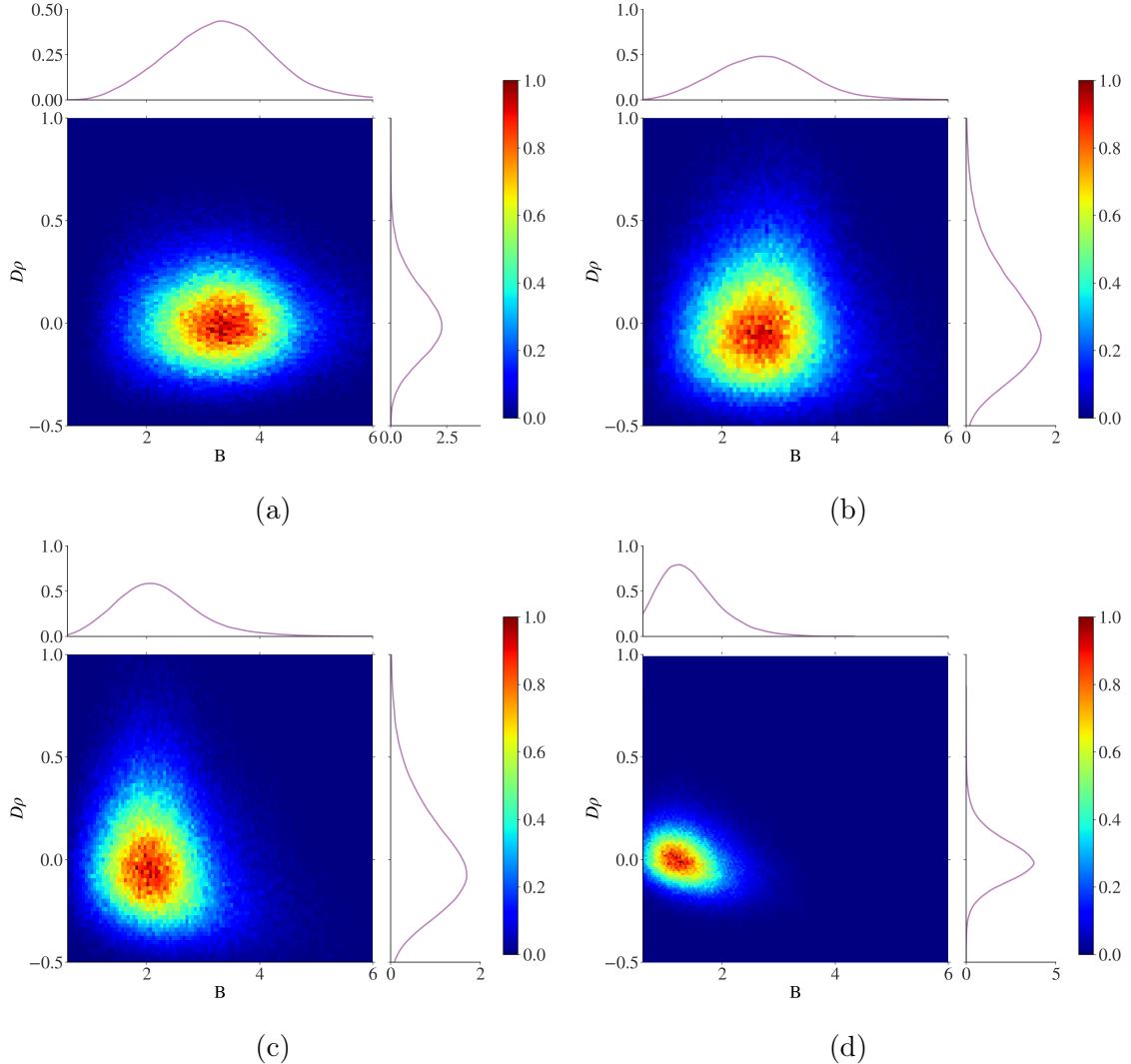


Figure 4.8: Slices representing the evolution of the heat maps of $D\rho$ and B in the simulation box at different redshifts $z = 3000, 1200, 900, 400$ respectively.

4.2 Simulation Results for Different Parameters

In our work we were able to run multiple simulations for different power spectra. We described both spectra in an earlier section. In this section we will discuss and interpret how the different initial conditions of the simulation affects it. We will first present the difference in the velocities for both cases at an initial magnetic field $B_0 = 1$.

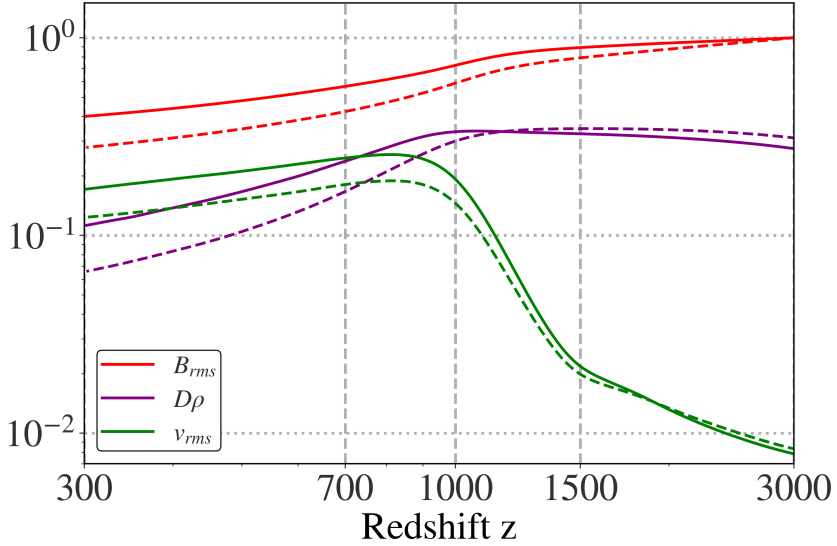


Figure 4.9: For $B_0 = 1$, the rms values of magnetic field (red), density perturbation (purple) and baryon velocity (green) are plotted as a function of redshift. Different initial magnetic spectra are shown: near scale-invariant (solid) and causal (dashed)

From figure (Fig. 4.9) one can see that the magnetic fields drops at a faster rate than the scale-invariant case. Both the velocity field and the density fluctuations start at values higher in the causal run. As expected the velocity field increases when the density fluctuations start to drop. We can see that the density fluctuations decay for causal faster than in scale-invariant case. Something interesting we see in this plots is that the magnetic energy decays faster for higher k , i.e. when the energy is stored in the smaller scales, we can see that they also decay to even lower values compared to having a low k . This plot confirms what was discuss earlier in the analysis chapter 2.2.

4.2.1 Scale-Invariant Cases

For the following plots, we present the results for the scale-invariant runs while varying the values of the initial magnetic field B_0 between (0.01-5) in codes units. For the highest magnetic field strength due to time constraints, the simulation is shown for a redshift of $z = 500$. However, since the simulation has passed through all the relevant cosmological regimes for this thesis, we decided to use it. Also there is the fact that our results do not describe the actual physics in the universe at redshifts lower than $z = 400$.

Variation of Initial Magnetic Amplitude Our simulations have varying magnetic field amplitude in the range $B_0 = (0.01–5)$. Here we investigate the behaviour of magnetic and kinetic amplitudes as well as dissipation and net heating rates as a function of varying initial magnetic field B_0 .

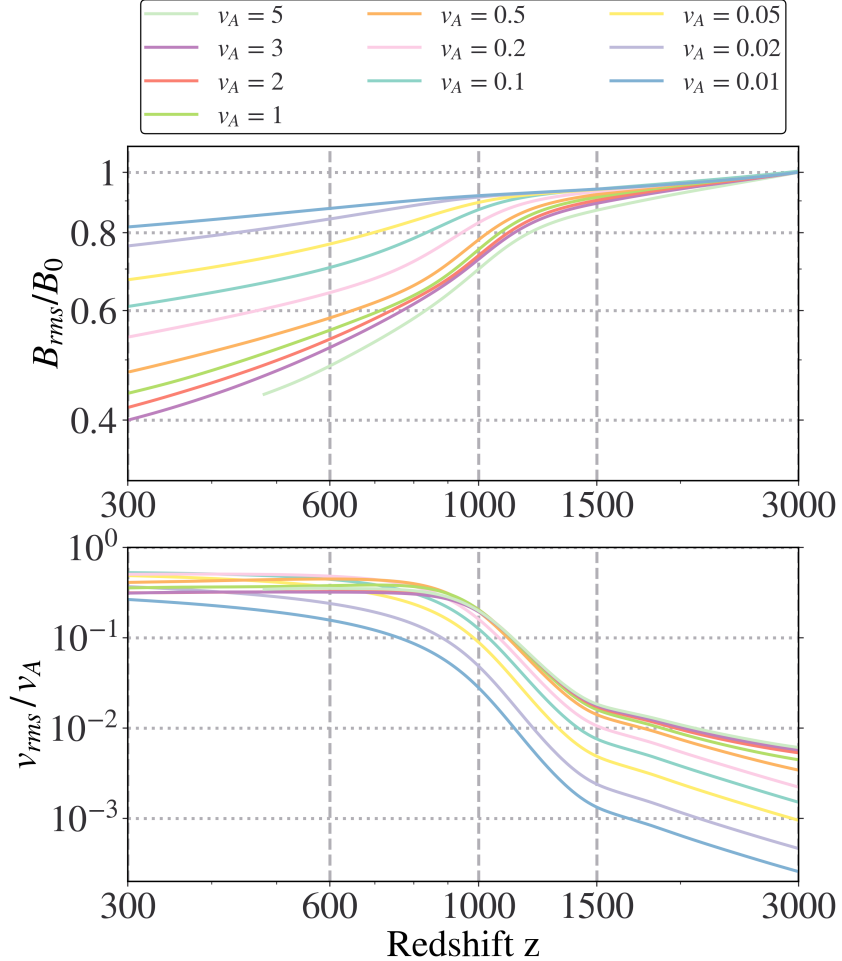


Figure 4.10: The redshift evolution of the rms magnetic field B_{rms} (top) and the rms velocity field v_{rms} (bottom), normalised to their values at $z = 3000$, for a range of PMF initial strengths

In the upper panel of figure (Fig. 4.10), we see that the high values of magnetic fields lose most of their strength through out the simulations. We can see that the highest magnetic field run $B_0 = 3$ loses almost 60% of its initial value, meanwhile the low magnetic fields conserve most of their strengths as seen for $B_0 = 0.01$ were we only see a drop of 18% of its initial value. In the early epochs, drag is causing a viscous regime which isn't allowing velocity field to form. When the drag no longer has this effect, v_{rms} rises. For

the higher B_0 values the Reynolds number reaches values that are higher than 10^3 , which causes the velocity field to become more turbulent.

In the lower panel, we can observe how v_{rms} evolves in the runs. The initial velocity field strength is clearly proportional to the value of B_0 . All the runs reach peak of their velocity fields at very similar redshifts $z = 800 - 900$. Which is where we saw in figure (Fig. 4.1) the peak of the kinetic energy. After reaching that point, the velocity fields start decaying as we enter the last regime in our runs.

Evolution of the Density Fluctuations We present in the following figure (Fig. 4.11) the evolution of the density perturbations in our runs. The fluctuations are computed using $D\rho = (\rho - \bar{\rho})/\bar{\rho}$.

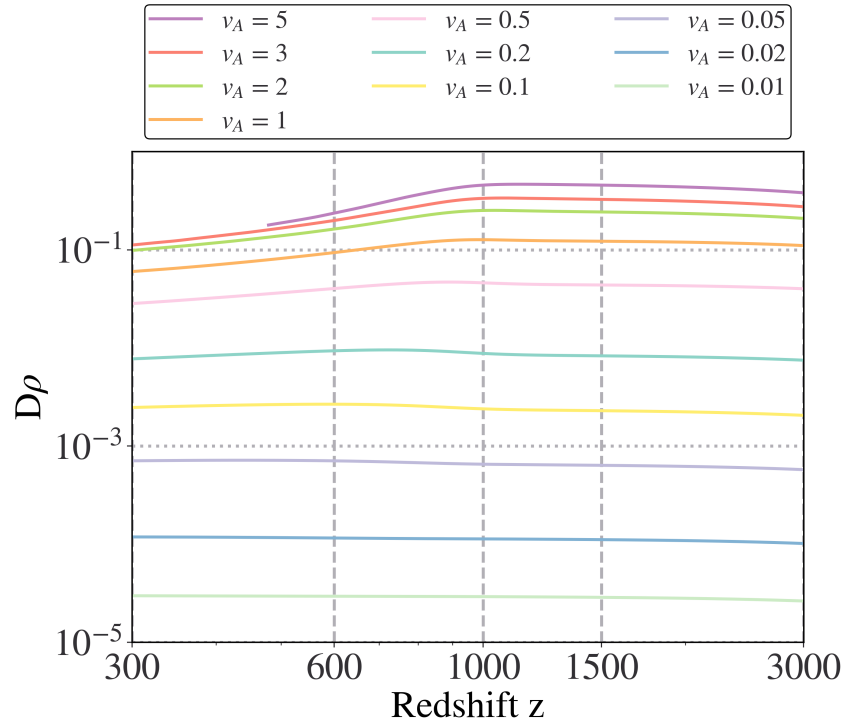


Figure 4.11: The redshift evolution of density perturbations for scale-invariant spectra magnetic fields over the range of PMF values from $B_0 = 0.01$ up to $B_0 = 5$

The density fluctuations are proportional to the initial value of the magnetic field, this is seen in the plot since for higher B_0 more density fluctuations are present. For high B_0 , $D\rho$ decays noticeably between redshift redshifts 300 – 1000, this is correlated with the fact that B_{rms}/B_0 drops significantly between these redshifts. For low B_0 , i.e. $B_0 < 0.1$,

the drop in B_{rms} is smaller, and therefore less energy is provided to the velocity field hence $D\rho$ doesn't decay; It actually increases. Appreciable turbulence is only created for the higher values of B_0 . From this plot, it is also clear that density perturbation although present in our runs never go towards non-linear structure regime.

Dissipation Rates We now study the difference in the magnetic dissipation and the net heating rate as a function of magnetic amplitude.

The magnetic energy density dissipated normalized to its peak value is plotted for different B_0 in the left panel of figure (Fig. 4.12). We only show the values from redshift $z = 2000$ since the earlier redshifts represent no physical meaning and are susceptible to numerical noise.

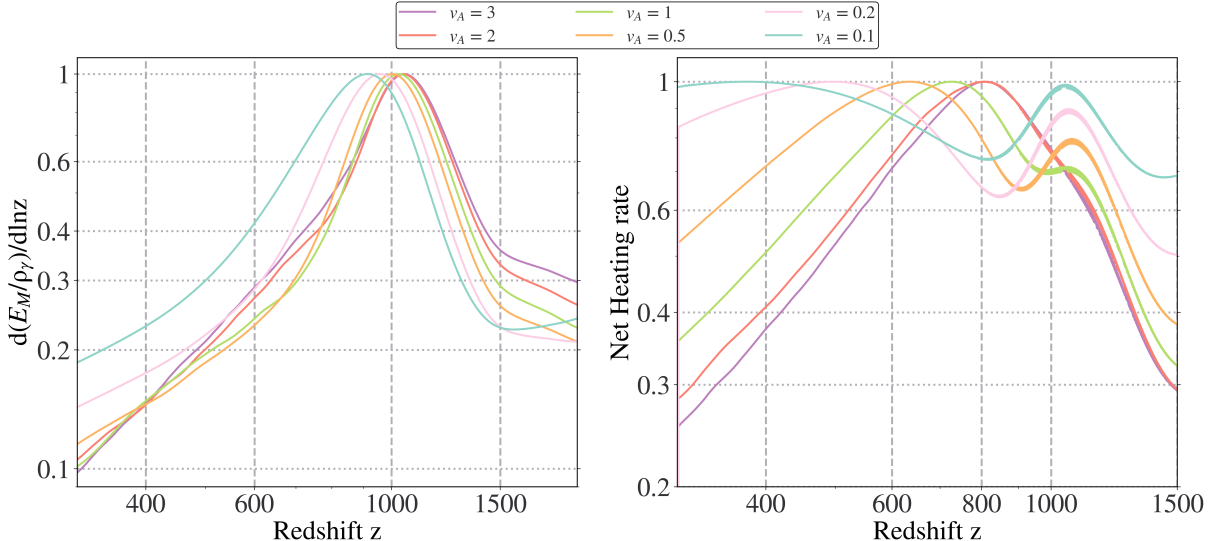


Figure 4.12: Comparison of the dissipation rate of both the magnetic energy density (left) and the net heating (right) for a range of PMF values from $B_0 = 0.01$ up to $B_0 = 3$. All curves are normalized to their peak amplitude.

We find that there is a redshift dependency for when the magnetic field dissipation actually peaks. The peak varies from values $z = 800 - 1100$. An interesting trend observed, is that the lower the initial magnetic field value, the more delayed the loss in the magnetic field. The reason behind that is that lower initial magnetic field, means lower initial v_{rms} , this results in longer time for velocity field to build up to its peak. This is also the reason why there is a delay for the values in the magnetic dissipation leak for the lower B_0 values.

The plot also shows us that for the lower end the curve has a broader range compared to the higher values of B_0 . This translates to a longer time for the second regime. The reasoning behind this delay is, the fact that the magnetic field is so weak. Since the only source of energy is the initial B field in our runs, this translates to a weak kinetic field, that takes longer to form, since the drag force still has a longer effect on the lower B_0 .

The net heating is computed by subtracting the dissipation due to drag ($2\tilde{\alpha}E_{\text{kin}}$) from the total energy dissipation rate ($dE_{\text{tot}}/d\ln z$). We showed earlier in figure (Fig. 4.3) the dissipation rate for all the different energies in our runs, E_{tot} , E_{mag} and E_{kin} as well as the drag and net heating dissipation rate for the scale-invariant case for $B_0 = 1$. We now show the different net heating dissipation for different initial magnetic field strengths also varying from $B_0 = 0.01 - 3$ in the right panel of the plot (Fig. 4.12). All the curves have been normalized to their maximum amplitude.

There are many interesting points to be discussed. We start by noting that at high B_0 , there is just one peak at redshift $z = 800$. Comparing this redshift value to the redshifts of when the magnetic field peaks we see a clear delay. This delay is due to the fact that the velocity fields need some time to form.

For the lower values of B_0 , the net heating begins by reaching a secondary maximum earlier before peaking at delayed redshifts compared to the higher B_0 values. The reason for these earlier peaks is due to how the drag force is evolving in the runs. The drag force is as we showed earlier $F_D = 2\alpha E_k$. With a constant α the only changing parameter is the kinetic energy in the runs. For low values, the kinetic energy is very weak thus causes the drag force to be weaker at earlier times compared to its value at high B_0 .

Using the data from the previous two plots we made a scaling plot to present the peak of the dissipation rate for the different fields. Figure (Fig. 4.13) shows a monotonic evolution for both curves. The reason behind not presenting the data for the lower net heating values is due to the fact that they do not peak. The values of the net heating dissipation at the low amplitudes are decaying from some initial value, this is also the reason why they are not shown for the earlier plot 4.12.

The best way to fit the data was dividing the plot into different sections and trying to get the best fit for each section. The data fit in the plot are shown in green for the maximum of the energy density dissipation and they are represented in (Eq. 4.4). In the best fit for the net heating dissipation rate, also presented in (Eq. 4.5). The fits in the plot have been displaced to make them easier to read.

$$\frac{d(Q_B/\rho_\gamma)}{d \ln z} = \begin{cases} 8.17 \times 10^{-11} \times B_0^{2.43}, & \text{for } 10^{-2} < B_0 < 10^{-1} \\ 6.08 \times 10^{-11} \times B_0^{1.82}, & \text{for } 10^{-1} < B_0 < 1 \\ 1.41 \times 10^{-11} \times B_0^{1.20}, & \text{for } B_0 > 1 \end{cases} \quad (4.4)$$

$$\frac{d(Q_{\text{net heating}}/\rho_\gamma)}{d \ln z} = \begin{cases} 2.32 \times 10^{-11} \times B_0^{2.02}, & \text{for } 10^{-1} < B_0 < 1 \\ 7.32 \times 10^{-12} \times B_0^{1.45}, & \text{for } B_0 > 1 \end{cases} \quad (4.5)$$

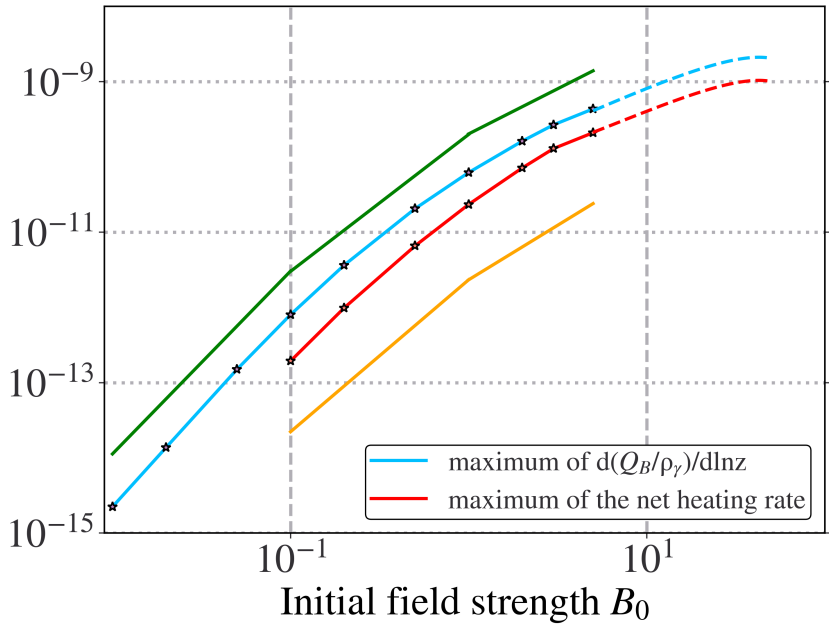


Figure 4.13: Peak values of the magnetic field $d(E_M/\rho_\gamma)/d \ln z$ and the net heating rate for different initial B_0 , and their fitting curves for the scale-invariant case

The equations show that the higher B_0 values have a lower power law index compared to the lower values of B_0 . We will discuss these values in more detail and compare them to other work later in section 5.

Since we were not able to run simulations with initial $B_0 > 0.2$ nG, we applied an extrapolation method to extract the evolution of the data for higher orders of magnitude, reaching initial $B_0 = 2$ nG. The extrapolation were done to these values, because they represent the upper limit to PMF set by the CMB power spectra (Planck Collaboration (2020)).

The dashed lines represent the extrapolation curves, equation 4.6 is shown in dashed blue and equation 4.7 is shown in dashed red.

$$\frac{d(Q_B/\rho_\gamma)}{d \ln z} = 7 \times 10^{-11} (B_0^{1.2} + 0.4B_0^{0.6} - 0.2B_0 - 0.052B_0^{1.81} - 0.0051B_0^2) \quad (4.6)$$

$$\frac{d(Q_{net\ heating}/\rho_\gamma)}{d \ln z} = 6.3 \times 10^{-11} (B_0^{1.2} + 0.7B_0^{0.3} - 0.7B_0 - 0.074B_0^{1.71} - 3 \times 10^{-4}B_0^{2.1}) \quad (4.7)$$

The trend found is what one would expect, the power law exponents keep dropping the higher the values of the magnetic field, to even reach a constant at the highest point.

Maximum Clumping Factor We present in the next figure (Fig. 4.14) the clumping factor for different initial B_0 . Since we are working with a stochastic initial magnetic field and negligible initial velocity field, the evolution of the velocities and the densities can be described by the Euler and the continuity equation as described by Jedamzik and Saveliev (2019):

$$\frac{\partial v}{\partial t} + (v \cdot \nabla) \cdot v + c_s^2 \frac{\nabla \rho_b}{\rho_b} = -\alpha v - \frac{1}{4\pi\rho_b} B \times (\nabla \times B) \quad (4.8)$$

$$\frac{\partial \rho_b}{\partial t} + \nabla(\rho_b v) = 0 \quad (4.9)$$

The following is true for a stochastic field: The fluid flows both rotational ($\nabla \times v \neq 0$) and compressible ($\nabla \cdot v \neq 0$). This compression leads to the formation of density fluctuations.

We define the clumping factor as the square of the maximum value of density perturbation $b = (D\rho)^2_{\max}$.

For the same reason as in the dissipation plot, we show an extrapolation of our data reaching $B_0 = 2$ nG in dashed blue. The equation used to show the curve is the following:

$$b = 3.5 \times 10^{-2} (B_0^{1.2} + 0.4B_0^{0.6} - 0.2B_0 - 0.052B_0^{1.81} - 5 \times 10^{-3}B_0^2) \quad (4.10)$$

This curve of the equation follows the trend seen in the plot, the values of b evolve slower and begin to shift from a power law similar to v_A^2 to only v_A .

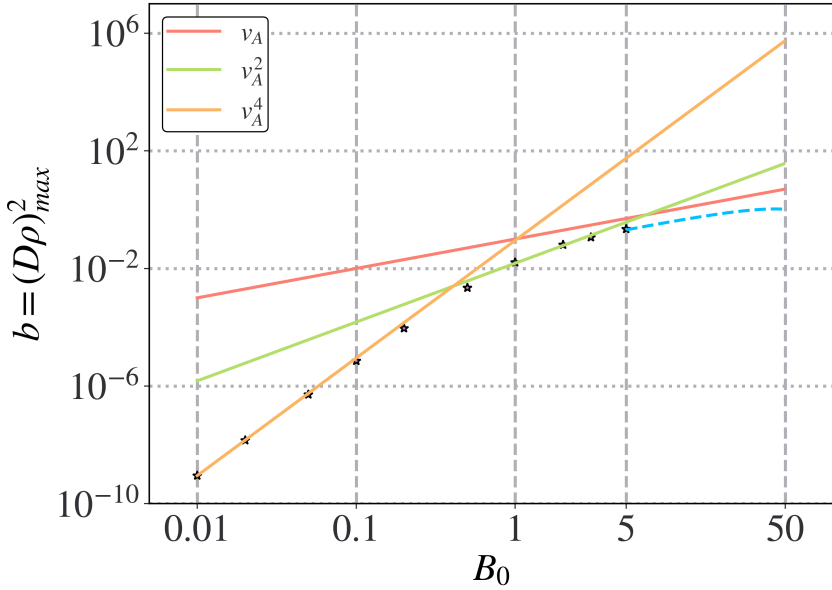


Figure 4.14: Comparison between the clumping factor for different initial magnetic field strengths for $B_0 = 0.01 - 5$ for the scale-invariant runs. The colored lines are fits for the data.

4.2.2 Causal Cases

As seen earlier in section 3, the causal case consists of a power law where the energy is stored at mid values of k ($k_{\text{peak}} = 10$). While working with this power spectra, we found that the maximum initial magnetic field we can reach is $B_0 = 3$. Any higher values of B_0 would cause our code to crash. We also found that the simulation of $B_0 = 3$ took a considerable amount of time compared to the scale-invariant case. This was due to a very small value of dt . The parameter dt in the code represents the amount of time between each time-step. In numbers the value of $dt = 1.96 \times 10^{-5}$ compared to the scale-invariant value of $dt = 5.15 \times 10^{-5}$. In the next few plots we will show the comparison of some physical parameters of our causal runs, the plots are broadly qualitatively similar to what we had for the scale-invariant case.

Variation of Initial Magnetic Amplitude First, we present the rms evolution the magnetic field evolve at different initial conditions in the upper panel of figure (Fig. 4.15). Comparing the values to the scale-invariant runs we see that the trend continues with the highest B_0 losing most of their initial conditions while the lower values are not very

affected at the end of the runs.

We can also see that the highest values of B_0 are more affected and reach a lower percentage of their initial values 28% compared to the 40% we saw in the scale-invariant cases.

The lower panel of the plot shows the evolution of the velocity field. As seen in the scale-invariant case, the initial value of this field is proportional to the initial magnetic field value B_0 .

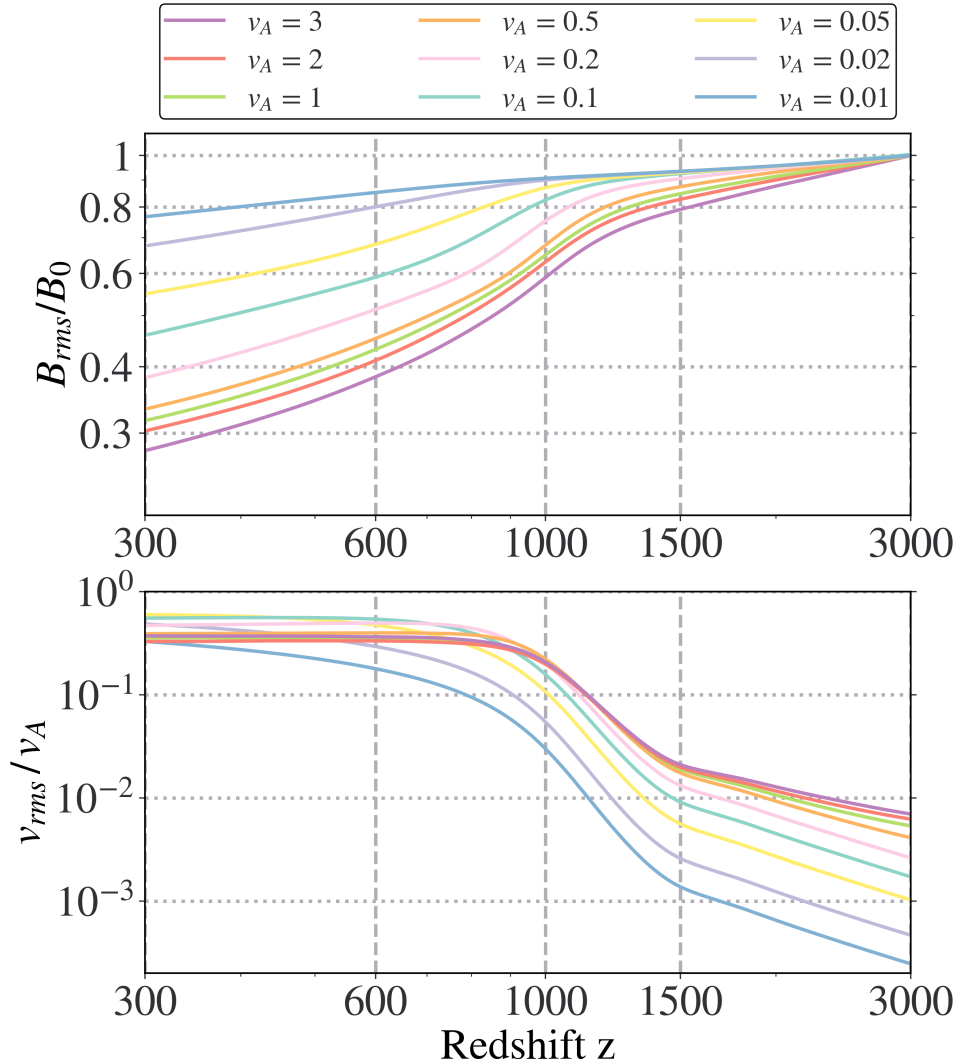


Figure 4.15: The redshift evolution of the rms magnetic field B_{rms} (top) and the rms velocity field v_{rms} (bottom), normalised to their values at $z = 3000$, for a range of PMF initial strengths $B_0 = (0.01 - 3)$

Evolution of the Density Fluctuations In the next figure (Fig. 4.16), the evolution of the density fluctuations for the causal runs are laid out. Both cases share similar trends and behaviors. At very low B_0 values, the density perturbations are very weak and remain as a constant throughout the run, they do however slightly reach values that are higher than their initial ones.

However for higher B_0 values, in both the photon drag regime and the beginning of the transition regime the density fluctuations show an increasing slope. The curves reach a maximum at times close to recombination, then begin to decay in the second half of the simulation. The behavior is easier seen at higher values of initial magnetic fields.

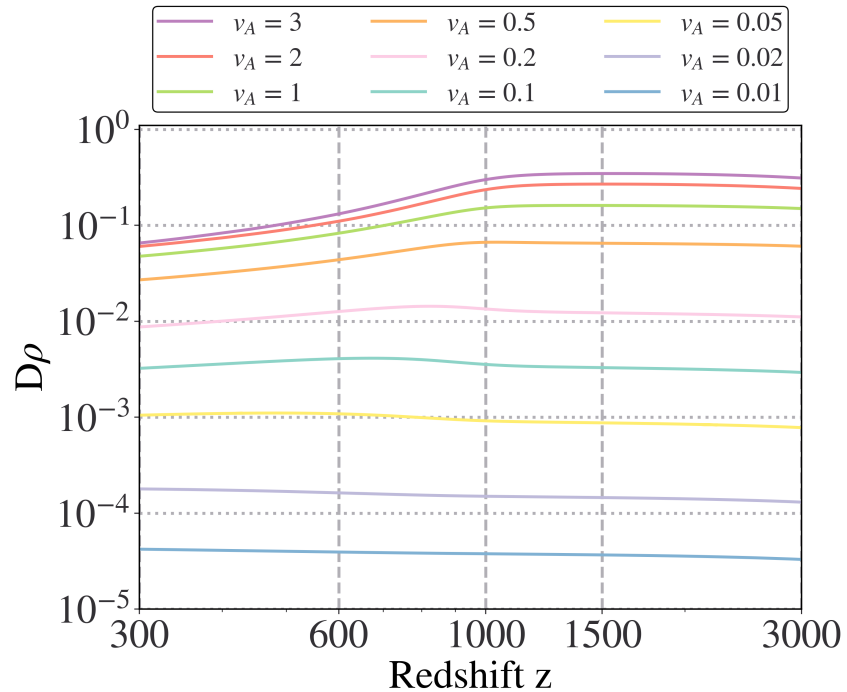


Figure 4.16: The redshift evolution of density perturbations for causal spectra magnetic fields over the range of PMF values from $B_0 = 0.01$ up to $B_0 = 3$

Comparing the initial and final values of the density fluctuations exhibits a bigger difference as to what is presented in the scale-invariant case. In that case, the final values of the fluctuations were only half their initial values. In the causal runs, the initial values are almost five times bigger than their values at the end of the simulation. Since there is a high loss of B_{rms} as seen in (Fig. 4.15), v_{rms} is rising to substantially values. These values of the velocity field causes more turbulent decay of $D\rho$, which causes them to decay so much.

Dissipation Rates The evolution of the net heating and the magnetic field dissipation in the causal runs are laid out in figure (Fig. 4.17). Looking into the magnetic dissipation plot (left panel), similar trends are present to the scale-invariant case. The plot is also cut at $z = 2000$, since at higher redshift values the plot doesn't represent any physical meaning and is only composed of numerical noise for the lower values of B_0 . The higher amplitude of magnetic fields enter the transition regime with a constant value, they then reach a maximum at recombination and decay for the rest of the simulation. As seen earlier, the peaks are delayed for the smaller values of B_0 . The peaks of the dissipation start as early as $z = 1100$ and end at $z = 800$ for the lowest value. For the lowest values, a broadening of the values of the energy dissipation is also observed.

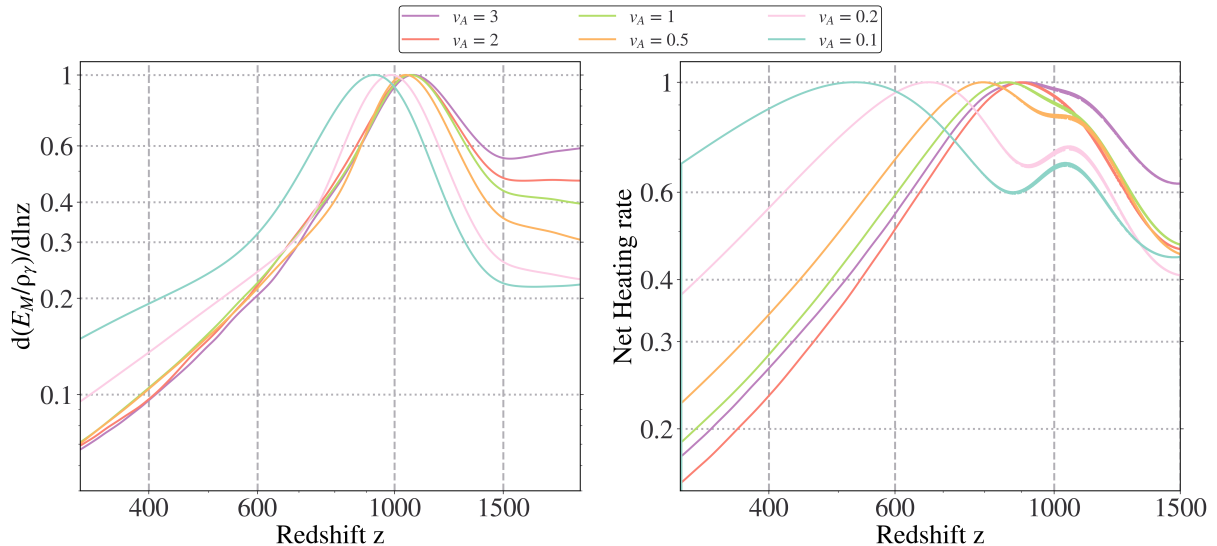


Figure 4.17: Comparison of the dissipation rate of the magnetic energy density for the causal type of magnetic spectra for a range of PMF values from $B_0 = 0.01$ up to $B_0 = 3$.

All curves are normalized to their peak amplitude.

The net heating is laid out in the right panel of figure (Fig. 4.17). For the high values of B_0 , a bump is seen earlier to the actual peak of the net heating, this is due to the drag force reaching a maximum before the total energy in the run. The same is seen for the lower values, however they are more expressed. This is due to the fact that the drag force is weaker in the lower runs compared to the higher B_0 values. The values of the net heating are reach in redshifts between $z = 500 - 900$. The net heating in this case reach a maximum earlier than the scale-invariant case.

The fits for the data of the maximum values of the net heating and the magnetic

field are presented in figure (Fig. 4.18), the equations expressing the curves are as follow:

$$\frac{d(Q_B/\rho_\gamma)}{d \ln z} = \begin{cases} 1.73 \times 10^{-10} \times B_0^{2.47}, & \text{for } 10^{-2} < B_0 < 10^{-1} \\ 1.09 \times 10^{-10} \times B_0^{1.80}, & \text{for } 10^{-1} < B_0 < 5 \times 10^{-1} \\ 3.11 \times 10^{-11} \times B_0^{1.31}, & \text{for } 5 \times 10^{-1} < B_0 < 2 \\ 6.67 \times 10^{-12} \times B_0^{0.60}, & \text{for } B_0 > 2 \end{cases} \quad (4.11)$$

$$\frac{d(Q_{\text{net heating}}/\rho_\gamma)}{d \ln z} = \begin{cases} 4.84 \times 10^{-11} \times B_0^{1.91}, & \text{for } 10^{-1} < B_0 < 5 \times 10^{-1} \\ 1.72 \times 10^{-11} \times B_0^{1.46}, & \text{for } 5 \times 10^{-1} < B_0 < 2 \\ 1.28 \times 10^{-12} \times B_0^{0.28}, & \text{for } B_0 > 2 \end{cases} \quad (4.12)$$

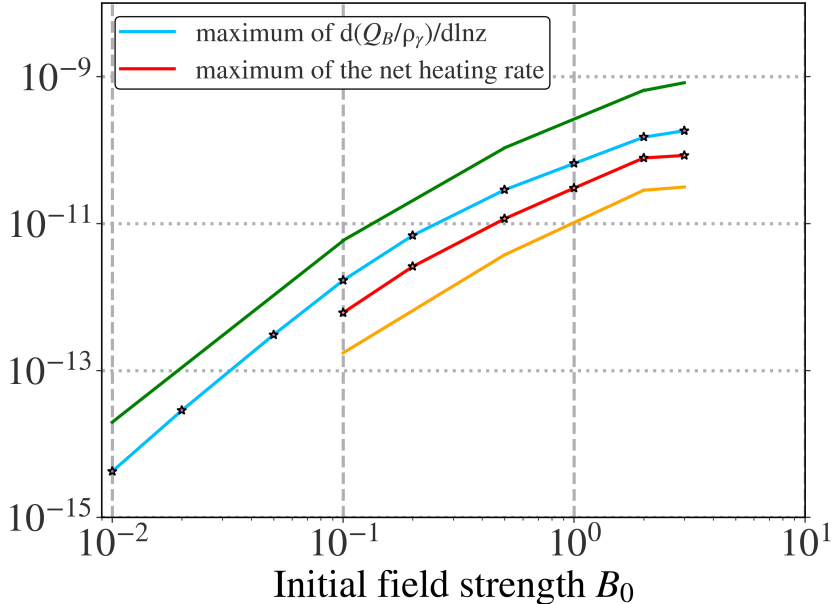


Figure 4.18: Peak values of the magnetic field $d(E_M/\rho_\gamma)/d \ln z$ and the net heating rate for different initial B_0 , and their fitting curves for the causal case

The fit for the curves were not a simple as we had for the scale-invariant runs. The maximum of the magnetic dissipation is divided to four parts, since we at the latest stage for $B_0 > 2$, there is a significant drop in the slope. The drop is also seen in the net heating, which is even of a lower slope.

Maximum Clumping Factor Lastly, we present the clumping factor for the causal case. The plot is very similar to the earlier scale-invariant run 4.14. The clumping factor for the lower B_0 values evolves with a slope of v_A^4 . The behavior at high values of B_0 is also similar to the scale-invariant case, where it begins to drop and the clumping factor evolves as v_A^2 .

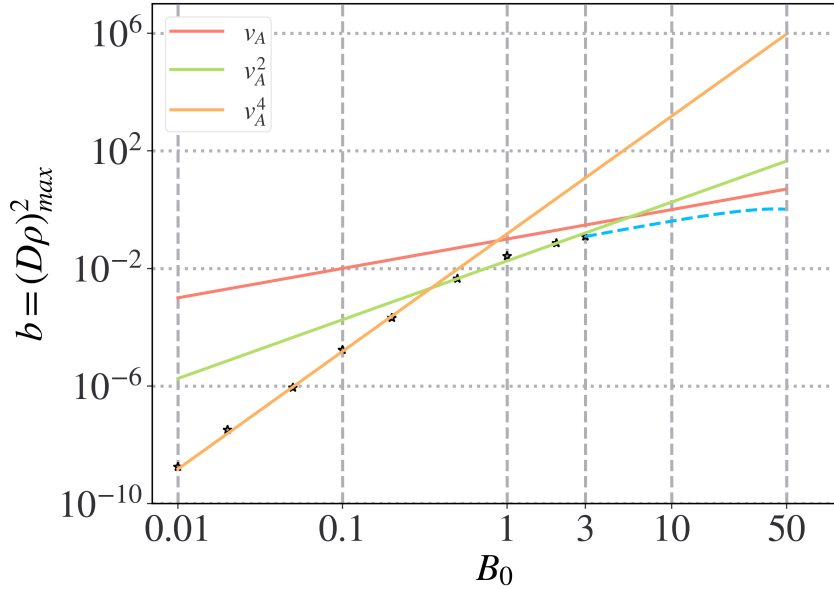


Figure 4.19: Comparison between the clumping factor for different initial magnetic field strengths for $B_0 = 0.01 - 3$ for the causal runs. The colored lines are fits for the data.

We also show the extrapolation of the data for the clumping factor b . The curve in blue is represented by the following equation:

$$b = 0.035(B_0^{-1.2} + 0.4B_0^{0.6} - 0.2B_0 - 0.052B_0^{1.81} - 5 \times 10^{-3}B_0^2) \quad (4.13)$$

The curve shows that the values of B_0 reaching the upper limit set by the CMB power spectra begin to lose amplitude and evolve as v_A .

Chapter 5

Discussion

In this section we will be discussing the physics in our runs. We will also compare our simulations and findings to other numerical and analytical works. We start by comparing our results to earlier numerical work. We later discuss our findings while equating for other analytical work. We lastly discuss some aspects of runs.

5.1 Numerical Comparison

The work done in this project can be compared to the numerical work done by Trivedi et al. (2018). In their work they were using the PENCIL code, the issue with that code was that they were limited to sub-sonic Alfvén velocities, that limited the range of their magnetic fields as they were able to reach a maximum $B_0 = 0.51$.

They were able to follow the evolution of the net heating and the magnetic energy field through their simulations. Comparing the values of the maximum dissipation we found in figure (Fig. 4.13), we find that the values in our work are systematically smaller. However, the differences in the power laws between the maximum of the magnetic field dissipation and the net heating dissipation is similar between both work. Due to the sourcing of the density fluctuations by the magnetic field in our runs, we observe smaller values of power laws in both the magnetic energy and the net heating dissipation (Equation 4.4).

Taking the sourcing of the density fluctuations into consideration, we observe very similar evolution of the rate of power law exponent with increasing initial magnetic field strength, as seen in table 5.1.

Table 5.1: Power law comparison for different spectra with Trivedi et al. (2018)

Spectra	$(Q_B)_\alpha$	(Net Heating) $_\alpha$	Ratio(%)
Scale-invariant ($0.01 < x < 0.1$)	1.82	2.02	90
Scale-invariant ($1 < x < 5$)	1.20	1.45	83
Causal ($0.1 < x < 0.5$)	1.80	1.31	94
Causal ($0.5 < x < 2$)	1.31	1.46	90
2018 (Scale-invariant)	2.26	2.55	89

The ratio represents the difference between the power law exponent for the net heating dissipation and the magnetic field dissipation. We assume that the density perturbations would play a role in reducing these exponents. Since the magnetic field is now sourcing a second output, compared to it only sourcing heating for the earlier work done in 2018. We find that at lower values of B_0 for scale-invariant and causal, the ratio to be the same at 90%, as in the 2018 work. That is reasonable since the density fluctuations were weak in these simulations.

However in the cases where B_0 is higher than 1 for scale-invariant, and where the density perturbations began to show presence in our runs, we find that the exponent actually drops to 83%. The drop is also seen in the values of causal between the lower and higher B_0 values.

5.2 Analytical Comparison

According to Subramanian (2016), the proper magnetic Jeans' wave-number in a linear analysis can be deduced using

$$4\pi G \rho_m = K_J^2 B^2 / (8\pi \rho_b) \quad (5.1)$$

Solving for K_J one gets:

$$K_J = \frac{4\pi \sqrt{2\rho_m \rho_b G}}{B} \quad (5.2)$$

Using the fact that $H^2(t) = 8\pi G \rho_m / 3$, the upper equation can be written as $K_J V_A(k_J, t) = \sqrt{3} H(t)$ taking into account the fact that $k_J = a K_J$.

We showed earlier that $V_A \propto a^{-1/2}$ in equation 2.5, and since $H(T) \propto t^{-1}$ thus $\propto a^{-3/2}$, we find that $k_J \propto a(t)H(t)/V_A$ is a constant with time. Putting in the number, one gets an analytical model (Subramanian; 2016) where

$$k_J = 14.8 \text{ Mpc}^{-1} \left(\frac{\Omega_m}{0.3} \right)^{0.5} \left(\frac{h}{0.7} \right) \left(\frac{B_J}{10^{-9}\text{G}} \right)^{-1} \quad (5.3)$$

Using this model with the numbers from our main simulation where $B_0 = 3$ code units = 0.12 nG, we get a value of the comoving jeans wave length $k_J = 123.33 \text{ Mpc}^{-1}$. Using this value we can also compute the Jeans length in this particular run: Since $\lambda_J = 2\pi/k_J = 2\pi/123.33 \text{ Mpc}^{-1} = 50 \text{ Kpc}$.

Putting these values in perspective, the wavelength of our power spectra are between $k = 2590 - 6.6 \times 10^5 \text{ Mpc}^{-1}$, and the physical size of our box $L_{\text{phys}} = 2.42 \text{ kpc}$ we computed earlier in section (3). This means that we are working with much smaller length scales than the magnetic field jeans lengths, which in turn translates to us working with potentially non linear density fluctuations, as they evolve down to much later epochs.

5.3 Open Questions

The following are some issues that need to be addressed. We begin by discussing the Alfvén damping scale, as it plays a important role in limiting the value of the initial B_0 allowed in our runs. We then discuss a solution to how we can solve this issue and some setbacks we found while implementing these modifications.

5.3.1 Alfvén Damping Scale

We compute the Alfvén damping wave-number by using the following equation by Subramanian (2016):

$$k_{\max} = 235 \text{ Mpc}^{-1} \left(\frac{B}{1 \text{ nG}} \right)^{-1} \left(\frac{\Omega_b h^2}{0.02} \right)^{1/2} \left(\frac{h}{0.7} \right)^{1/4} \quad (5.4)$$

The cosmological constants used are taken from the Planck Collaboration (2020) where $\Omega_b = 0.0223$ is the baryonic density fraction and $H_0 = 67.4 \text{ km/s}$ the value of the Hubble parameter. To interpret these values it is best to compare them for different values of the initial magnetic field strengths, this is done in table 5.2. The values of Alfvén

wave-number allow us to understand how much damping our power spectra will undergo. The damping depends on the value of $k_{d,A}$ compared to the k_{phys} we computed earlier in section 3.

$$k_{\text{phys}} = 2\pi/L_{\text{phys}} = 2590(h/0.7) \text{ Mpc}^{-1} \quad (5.5)$$

$$k_{\text{res}} = (N/2)k_{\text{phys}} = 6.6 \times 10^5(h/0.7) \text{ Mpc}^{-1} \quad (5.6)$$

Table 5.2: The Alfvén damping wave-number and percentage of the density perturbations total energy damped at recombination for different initial magnetic field strengths

B_0 (code)	B_{phys} (nG)	$k_{d,A}$ (Mpc^{-1})	Energy damped (%)
5	0.2	1260	100
3	0.12	2100	100
2	0.078	3150	99.91
1	0.039	3600	99.82
0.1	3.9×10^{-3}	6.3×10^4	74.78
0.01	3.9×10^{-4}	6.3×10^5	1.33

The range of k_{phys} we computed earlier is between $(2590 - 6.6 \times 10^5) \text{ Mpc}^{-1}$. The higher values of $B_0 = (3-5)$ seem to be possibly totally damped, meanwhile for the lower values the damping wave-number is situated in the middle of our range of k_{phys} . The percentage of energy damped is computed by integrating the power spectra of the density fluctuations at recombination ($z=1100$), while taking into account where the position of $k_{d,A}$. With configuration used, the damping is setting a sub-sonic restriction to our simulations. We discuss in the next section a measure we took to solve this issue and its results.

5.3.2 Different Box Sizes

The only solution to avoid the damping is to change the value of k_{phys} . This is done by increasing the box size. We ran multiple simulations where $B_0 = 1$, varying the box size to study its effect on the simulations. The results of the boxes with different sizes were very similar to the box used in the main configuration.

The highest box size we were able to simulate was $L = 5$ (code unit); this was the maximum the code was able to handle without crashing. The crash only occurred after the modifications to the density perturbations and the drag force were applied. Thus implying, that the drag force might have been the reason. Since it has a strong effect on the evolution of the fields.

Using a bigger box size means the new box size, physical wave-number and resolution wave-number will all get affected. We show the following values for $L = 5$:

$$L_{phys} = 12.1(h/0.7)^{-1} \text{ kpc} \quad (5.7a)$$

$$k_{phys} = 519(h/0.7) \text{ Mpc}^{-1} \quad (5.7b)$$

$$k_{res} = 1.32 \times 10^5(h/0.7) \text{ Mpc}^{-1} \quad (5.7c)$$

The change in the box size will affect how much the density perturbations power spectra will get damped. For the box with length $L = 5$, we find that with initial magnetic field $B_0 = 1$, the percentage of damping drops from 99.82% (for $L = 1$) to only 21.66% (for $L = 5$). Changing the box size removes the sub-sonic restraint that the damping has on our simulations.

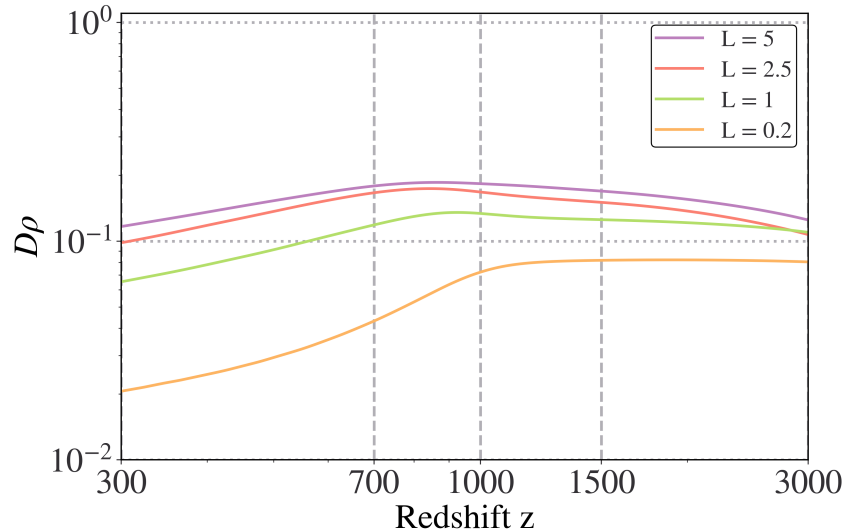


Figure 5.1: The evolution of density fluctuations for different box sizes for $B_0 = 1$ resolution $N = 256$ and the scale-invariant power spectra.

Increasing the box size had however some effects on some of the physical parameters

in the run. Most notably changing the box size also affected the density perturbations. This is an issue, since we would expect density perturbations to remain constant.

In figure (Fig. 5.1), the density fluctuations are shown at a resolution of $N = 256$, for the scale-invariant spectra. The box sizes was varied to check how it would affect different physical parameters. There are some variations in the $D\rho$ evolution, all fields begin from a very similar initial value and evolve to what is seen in the plot. The reason behind these variations is still unclear. The shape of the lowest box value is the most confusing since even for values that are as low as $B_0 = 0.01$, the behavior is different. The interpretation of this result and further tests are left for the future work.

Chapter 6

Conclusion

In this work we ran 3D MHD simulations of primordial magnetic fields across different cosmological regimes. We also followed the evolution of multiple physical parameters such as the heating, the baryonic velocity field as well as the density perturbations. The photon drag we used is the standard recombination history that we obtained from *CosmoRec* (Chluba and Thomas; 2010).

We found different regimes in our runs. Starting with the photon drag dominated regime, which begins at the start of the simulation until a redshift $z = 1500$. The second regime we call the transition regime, it lasts from redshift $z = 1500$ until $z = 700$, the end of this regime varies on how strong the initial magnetic field that we use; The stronger the field the earlier this regime ends. The last regime in our runs is the turbulent decay and it starts from when the transition regime ended and remains until the end of the simulations.

The baryonic velocity field in the run was found to be strongly suppressed at early times, that is due to the strong drag force at that time. They remain weak until the start of the second regime when the drag force weakens as seen in (Fig. 3.2). After entering this phase, we see them explode and greatly increase in value. That is the cases until they reach the final regime and saturate at a constant value for the rest of the simulation.

The density fluctuations were also studied in this work. We found them to be non dominant in our runs. At the beginning of the simulations the values of $D\rho$ are strongly dependent on the initial value of the magnetic field B_0 , and as we found in (Fig. 4.14), they evolve as B_0^2 . Their evolution also depends on the strength of the initial magnetic field, as we see them constant for the lower end. For the higher end we see them reaching

a maximum in the second regime until they drop to values lower than their initial values in the decay regime.

We also found in the PDF of the density fluctuations that they are non Gaussian. Both skewness and kurtosis tests were applied to study their distribution, and we found large amount of kurtosis at the early redshifts $z = 3000$.

The net heating evolution was also carefully studied throughout the run. We observe it to be non existing in the photon drag regime. However, as soon as the transition regime starts we see the net heating beginning to show in the run and increase in amplitude until it reaches a maximum around redshifts $z = [600 - 700]$. We later see it decay during the last regime. The shapes that we get for the net heating are broader than what previously estimated with a semi-analytical approach. We also found that the net heating is delayed by $z = 200$ from when the magnetic field dissipation reaches its maximum. There also delays in the net heating between different simulations depending on the strengths of the initial magnetic field.

We discussed the Alfvén damping and its effect on the simulations, and an approach to solving the damping of the highest initial B_0 runs. The approach taken to solve the issue was to increase the box size, thus decreasing the k_{\max} . However doing so changed some output parameters in our results, most importantly density fluctuations. This is due to the fact that while writing the code, the box size was considered to be a constant, since we didn't think that we'll be changing it. Some changes to the code need to be addressed to solve this issue.

Bibliography

- Banerjee, R. and Jedamzik, K. (2004). Evolution of cosmic magnetic fields: From the very early universe, to recombination, to the present, *Phys. Rev. D* **70**: 123003.
URL: <https://link.aps.org/doi/10.1103/PhysRevD.70.123003>
- Bernet, M. L., Miniati, F., Lilly, S. J., Kronberg, P. P. and Dessautes Zavadsky, M. (2008). Strong magnetic fields in normal galaxies at high redshift, *Nature* **454**.
URL: <https://doi.org/10.1038/nature07105>
- Brandenburg, A., Kahniashvili, T. and Tevzadze, A. G. (2015). Nonhelical inverse transfer of a decaying turbulent magnetic field, *Phys. Rev. Lett.* **114**: 075001.
URL: <https://link.aps.org/doi/10.1103/PhysRevLett.114.075001>
- Brandenburg, A., Sokoloff, D. and Subramanian, K. (2012). Current status of turbulent dynamo theory, *Space Science Reviews* **169**(1-4): 123–157.
- Charbonneau, P. (2014). Solar dynamo theory, *Annual Review of Astronomy and Astrophysics* **52**.
- Chluba, J. and Thomas, R. M. (2010). Towards a complete treatment of the cosmological recombination problem, *Monthly Notices of the Royal Astronomical Society* p. noâ€“no.
URL: <http://dx.doi.org/10.1111/j.1365-2966.2010.17940.x>
- Collaboration, T. P. (2020). Planck 2018 results. vi. cosmological parameters.
- Durrer Ruth, N. A. (2013). Cosmological magnetic fields: their generation, evolution and observation, *Reports on Progress in Physics* **21**.
URL: <https://doi.org/10.1007/s00159-013-0062-7>
- Finelli, F., Paci, F. and Paoletti, D. (2008). Impact of stochastic primordial magnetic fields on the scalar contribution to cosmic microwave background anisotropies, *Phys.*

Rev. D **78**: 023510.

URL: <https://link.aps.org/doi/10.1103/PhysRevD.78.023510>

Furlanetto, S. R. and Loeb, A. (2001). Intergalactic magnetic fields from quasar outflows, *The Astrophysical Journal* **556**(2): 619–634.

URL: <https://doi.org/10.1086/321630>

Harrison, E. (1973). Origin of magnetic fields in the early universe, *Physical Review Letters* **30**(5): 188.

Hathaway, D. H. and Rightmire, L. (2011). Variations in the axisymmetric transport of magnetic elements on the sun: 1996–2010, *The Astrophysical Journal* **729**(2): 80.

Jedamzik, K., Katalinić, V. c. v. and Olinto, A. V. (1998). Damping of cosmic magnetic fields, *Phys. Rev. D* **57**: 3264–3284.

URL: <https://link.aps.org/doi/10.1103/PhysRevD.57.3264>

Jedamzik, K., Katalinić, V. c. v. and Olinto, A. V. (2000). Limit on primordial small-scale magnetic fields from cosmic microwave background distortions, *Phys. Rev. Lett.* **85**: 700–703.

URL: <https://link.aps.org/doi/10.1103/PhysRevLett.85.700>

Jedamzik, K. and Saveliev, A. (2019). Stringent limit on primordial magnetic fields from the cosmic microwave background radiation.

Kandus, A., Kunze, K. E. and Tsagas, C. G. (2011). Primordial magnetogenesis, *Physics Reports* **505**(1): 1 – 58.

URL: <http://www.sciencedirect.com/science/article/pii/S0370157311000536>

Kulsrud, R. M., Cen, R., Ostriker, J. P. and Ryu, D. (1997). The protogalactic origin for cosmic magnetic fields, *The Astrophysical Journal* **480**(2): 481.

Neronov, A. and Vovk, I. (2010). Evidence for strong extragalactic magnetic fields from fermi observations of tev blazars, *Science* **328**(5974).

URL: <http://dx.doi.org/10.1126/science.1184192>

Oslon, P. (2013). The geodynamo's unique longevity, **66**.

URL: <https://doi.org/10.1063/PT.3.2177>

Paoletti, D., Finelli, F. and Paci, F. (2009). The scalar, vector and tensor contributions of a stochastic background of magnetic fields to cosmic microwave background anisotropies, *Monthly Notices of the Royal Astronomical Society* **396**(1).

URL: <http://dx.doi.org/10.1111/j.1365-2966.2009.14727.x>

Sethi, S. K. and Subramanian, K. (2005). Primordial magnetic fields in the post-recombination era and early reionization, *Monthly Notices of the Royal Astronomical Society* **356**(2): 778–788.

URL: <https://doi.org/10.1111/j.1365-2966.2004.08520.x>

Shaw, J. R. and Lewis, A. (2010). Massive neutrinos and magnetic fields in the early universe, *Phys. Rev. D* **81**: 043517.

URL: <https://link.aps.org/doi/10.1103/PhysRevD.81.043517>

Subramanian, K. (2006). Primordial magnetic fields and cmb anisotropies, *Astronomische Nachrichten* **327**: 403–409.

URL: <https://onlinelibrary.wiley.com/doi/abs/10.1002/asna.200610542>

Subramanian, K. (2016). The origin, evolution and signatures of primordial magnetic fields, *Reports on Progress in Physics* **79**(7): 076901.

URL: <https://doi.org/10.1088/0034-4885/79/7/076901>

Subramanian, K. and Barrow, J. D. (2002). Small-scale microwave background anisotropies arising from tangled primordial magnetic fields, *Monthly Notices of the Royal Astronomical Society* **335**(3): L57–L61.

Trivedi, P., Reppin, J., Chluba, J. and Banerjee, R. (2018). Magnetic heating across the cosmological recombination era: Results from 3d mhd simulations, *Monthly Notices of the Royal Astronomical Society* **481**(3): 3401–3422.

Wasserman, I. (1978). On the origins of galaxies, galactic angular momenta, and galactic magnetic fields, *The Astrophysical Journal* **224**: 337–343.

Appendices

Appendix A

Simulation Parameters

As any typical Flash script, the files are divided into the usual .F90 files, config and flash.par files. In the following one can find the parameter file used for the $N = 512$ and $B_0 = 1$ run.

```
#Cosmology
z = 300-5000
#Friedmann solution
solution_type = a ~ exp(2/3 t)
UnitSystem = "CGS"
rho_unit = 1.0
pres_unit = 1.0
sndspd = 1.0
alfven_vel = 1
gamma = 1.0001
#Resolution
N = 512
#Simulation parameters
cfl = 0.4
lrefine_min = 7
lrefine_max = 7
```

Appendix B

Detailed Results and Tests

In the following, a series of useful plots that did not appear in the thesis are laid out. These plots were not presented in the thesis because they wasn't much to be said, nevertheless we believe they are of importance and should be presented.

B.1 Resolution Comparison

Beginning with the resolution comparison for the scale-invariant cases. Since this parameter was constrained in our runs to $N = 512$, our approach was to show that a comparison between the resolutions that our runs are able to achieve and show that differences between these resolutions are minor.

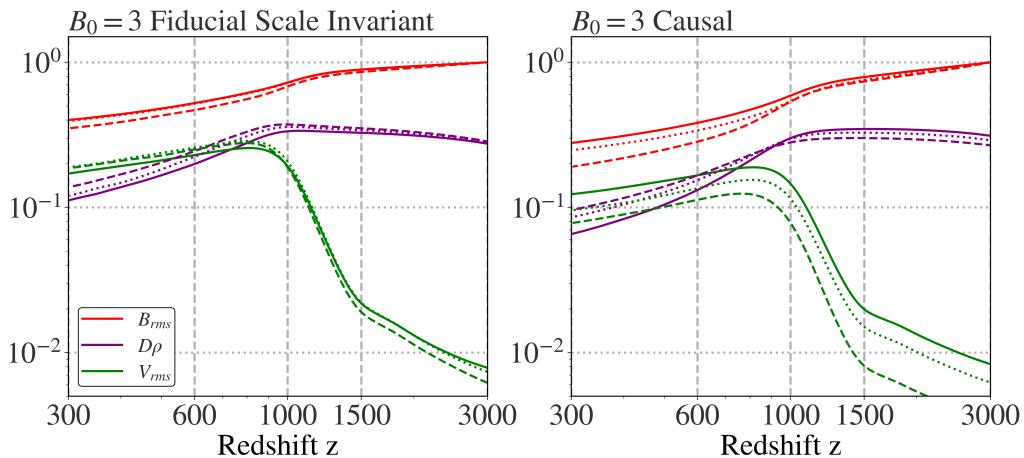


Figure B.1: Resolution comparison for the fiducial power spectra for an initial magnetic fields $B_0 = 3$ (left), and for the causal $B_0 = 3$ (right).

The plot (Fig. B.1) is presented with 3 curves shown for 3 different resolution. On the left panel a comparison for $B_0 = 3$ for the scale-invariant initial power spectrum and on the right panel a comparison for $B_0 = 3$ with a the causal in initial conditions. The dashed lines represent the lowest resolution of $N = 128$, the dotted lines represent $N = 256$, and the straight lines are for the highest resolution $N = 512$. From the plot, it is clear and safe to say that although the resolution does affect our runs. Even though the higher the resolution the more physics can be resolved in our runs, the lower runs show a very good description of how the physics would unfold in the box.

B.2 Bigger Box Run

We showed earlier that Alfvén damping was causing an issue in our runs, and was restricting our data to be only sub-sonic. The solution to the issue was to change the size of box we were working with. We experimented with multiple box sizes, ranging the box from $L = (0.2 - 2.5 - 5)$. Doing these changes wasn't as trivial as one thinks, since our code was written with a box size of $L = 1$ in mind.

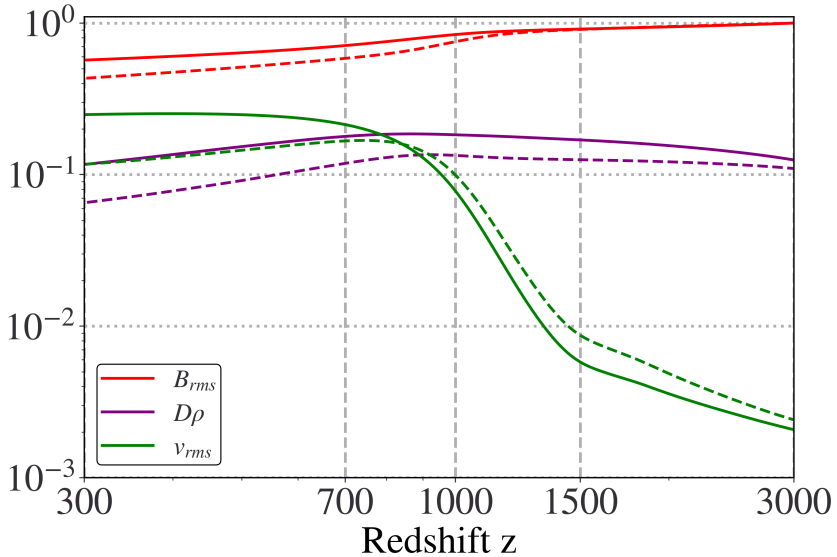


Figure B.2: Comparison of the rms fields for different box sizes. The dashed lines represent $L = 1$, the solid line represents $L = 5$

Figure (Fig. B.2) shows the evolution of the fields for the same initial $B_0 = 1$. The dashed lines represent the main configuration we had in the manuscript, and the normal lines represent the bigger box. Due to time constraints, we were not able to simulate a

higher resolution box of size $L = 5$, for the bigger box the resolution is only $N = 256$. However, we showed earlier that the change in resolution from $N = 256$ to $N = 512$ had a very minimal change on the physics in our runs. With higher resolution we think that the box would have a very similar behavior of what is shown in the figure.

The velocity figure shows an increase in the density fluctuations, this is not expected. As per usual, B_{rms} have both been normalised to their values at $z = 3000$. B_{rms} of the main configuration evolves much faster in than for the bigger box. The rms velocity field begins at higher values in the small box but evolves slower in the transition regime. v_{rms} in the bigger box reach higher values and do not display any decay in the turbulent regime.

B.3 Causal Power Spectra

Magnetic and Kinetic Spectra The upper panel of figure (Fig. B.3) shows the evolution of the magnetic field. At early redshifts, the energy is present at the peak value of the wave-number which is what defines our causal spectra.

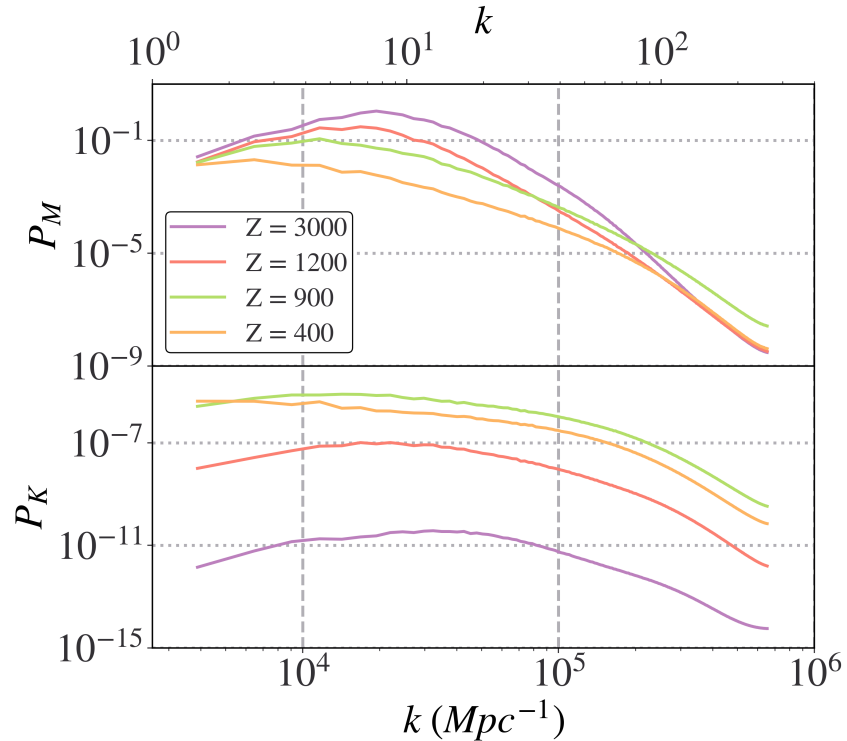


Figure B.3: Redshift evolution of the power spectra of magnetic and velocity field for the causal spectra with $B_0 = 3$

However as redshifts reach recombination and the second regime, the shape of the power spectra changes and takes the shape of a power law this is a sign of turbulence.

The peak of the curve shifts to the left, to bigger scales meanwhile at redshift $z=900$ presents an increase in small scales. At the end of the run, the power spectra has decayed into almost a straight line.

For the lower panel, the evolution is as expected, there is an increase in the power spectra due to the increase in the value of v_{rms} during the second regime. This is true until the last regime, where the velocity fields decays.

Density Fluctuations Spectrum The density fluctuations power spectra presents a slope very similar to the magnetic field at early redshift. The power law then shifts to a higher values of at the high scales, and keep the same shape at the lower scales. The final redshift represents the decay where the density fluctuations drop to very small values but keep the same power law.

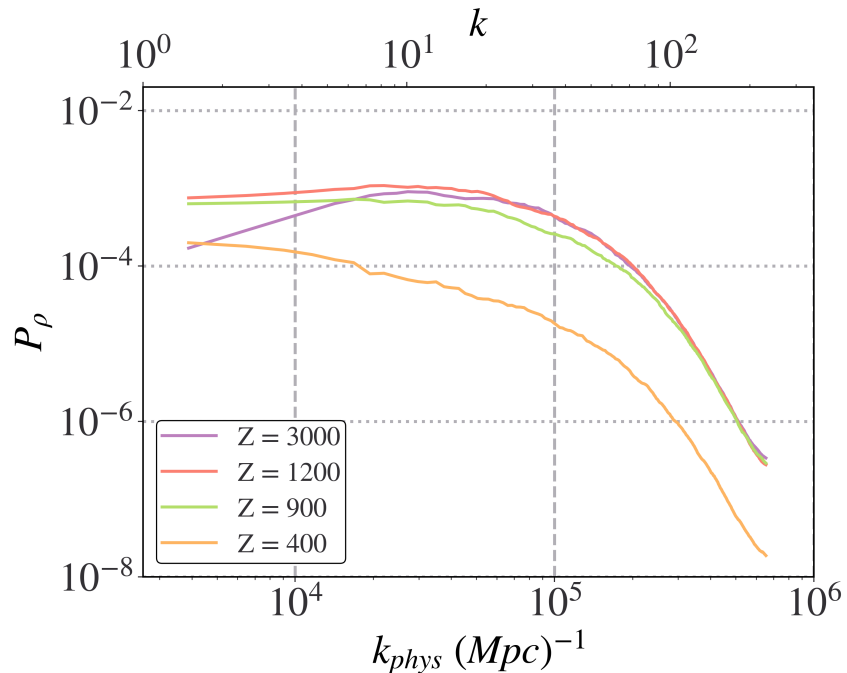


Figure B.4: Redshift evolution of the power spectra of density fluctuations for the causal spectra with $B_0 = 3$

B.4 Null Initial Field

For good measurement, we ran a simulation with a field that had an initial magnetic field strength of $B_0 = 0$. Since the initial field is 0, there are no field to source any of our physical parameters. So what we expect is a run where all the physical parameters in our run are null. After running the simulation and applying all the necessary modifications discussed earlier, we indeed find that all the physical terms in our runs are null.

B.5 Reynolds Number

The following plot represents the Reynolds number for the scale-invariant cases. It is computed using the following equation:

$$Rm = \frac{v_A}{\tilde{\alpha} L} \quad (\text{B.1})$$

The plot shows that all of the fields reach a unity value of the Reynolds number at redshifts close to $z=600$. This represents when the turbulent decay sets.

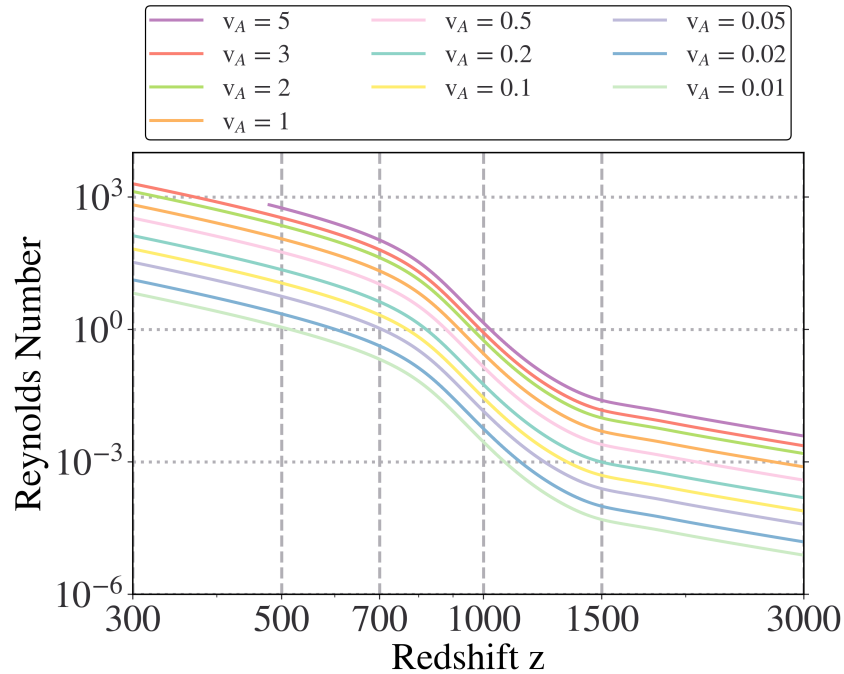


Figure B.5: Redshift evolution of Reynolds number for the scale-invariant spectra with $B_0 = 3$

B.6 Dependence of initial B on k_{\max} ?

We created different cases of scale-invariant spectra with varying k_{\max} to test the hypothesis whether the maximum k-scale in the scale-invariant spectra is the one that sets the value of $D\rho$. The hypothesis arises from the argument that due to the divergence of the Lorentz Force $S_0 \simeq (kB)^2$, the $D\rho$ value will be set by the scale-invariant spectrum's k_{\max} rather than its entire k-range. The interpretation of results and further tests are left for the future work.

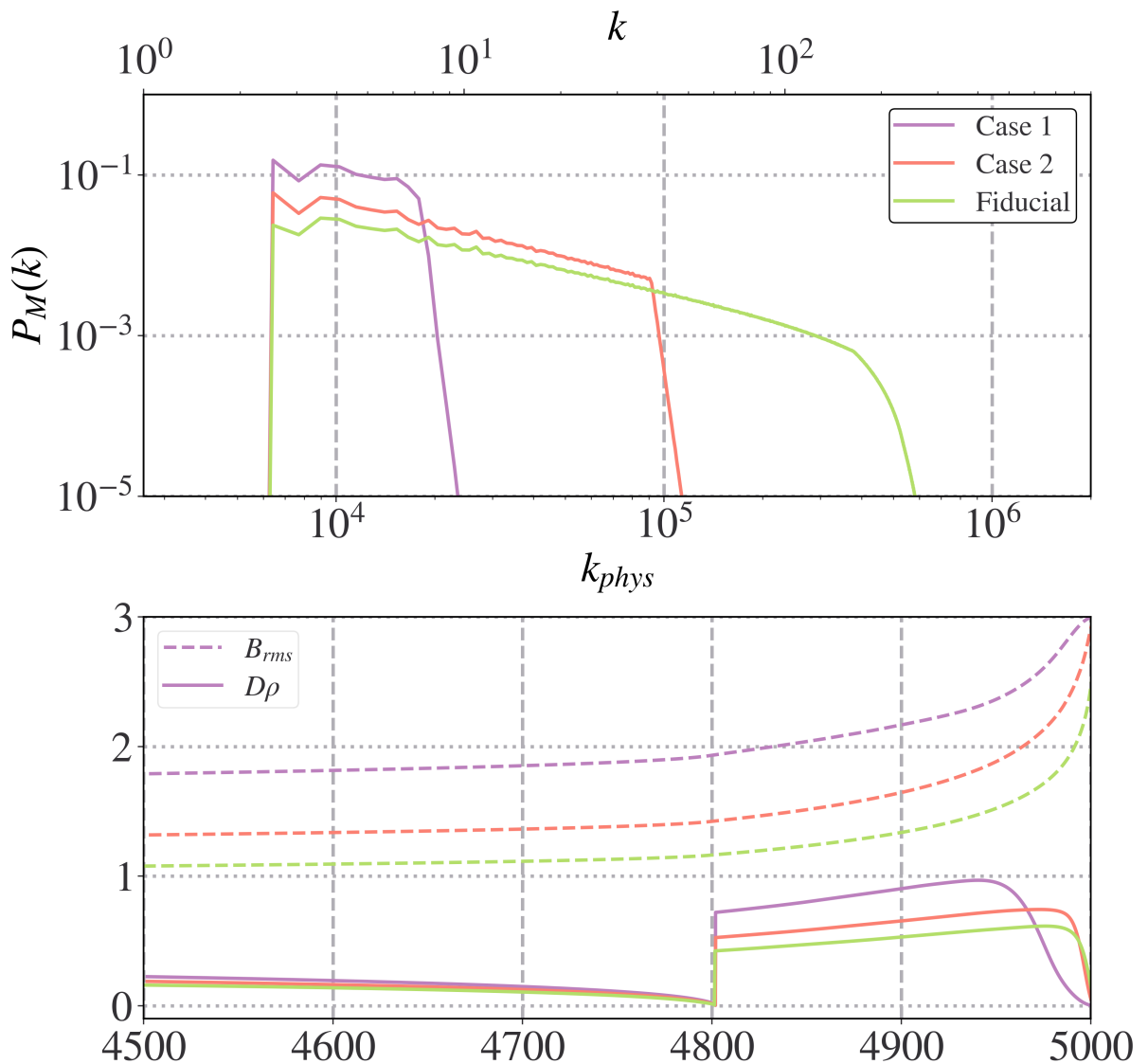


Figure B.6: Evolution of the power spectra (upper panel), the rms magnetic field strength and the density fluctuations (lower panel) for the different cases

The approach we decided on was to divide the power spectra into:

- Case 1: $P_M(k) = 0$ for $k > 10$ (Working with large length-scale power only)
- Case 2: $P_M(k) = 0$ for $k > 50$ (Working with intermediate length-scale power only)
- Case 3: The power spectra we were using for the scale-invariant runs.

The power spectra we used to test this hypothesis are in the upper panel of figure (Fig. B.6). We tried changing the values of k_{\max} to 10,60,256 respectively. The simulations we ran were only between redshift 4500 and 5000. At $z = 4800$, the density reset is seen, this has been applied in all the runs due to the grid structures. Again, we just showcase the tests we made, but leave their interpretation for later work.

Appendix C

Scripts Used

The power spectra function used in the next script is a modified approach to the YT cookbook. There were some changes to study the power spectra from our runs. The next function studies the power spectra of the density fluctuations. As mentioned in Chapter 3 there is difference of $a = 1/2\pi^3$ between these scripts and the ones for the initial magnetic field created by the IDL scripts.

Power Spectrum

```
import yt
import numpy as np

def doit(ds, fieldUsed):

    # a FFT operates on uniformly gridded data. We'll use the yt covering grid
    # for this.

    max_level = ds.index.max_level
    low = ds.domain_left_edge
    dims = ds.domain_dimensions*2**ds.max_level)
    nx, ny, nz = dims
    Kk = np.zeros((nx // 2 + 1, ny // 2 + 1, nz // 2 + 1))

    for i in range(3):
```

```

Kk += 0.5* fft_comp(
    ds, ("gas", fieldUsed), nindex_rho, max_level, low, dims, i
)

# wavenumbers
L = (ds.domain_right_edge - ds.domain_left_edge).d

kx = np.fft.rfftfreq(nx) * nx / L[0]
ky = np.fft.rfftfreq(ny) * ny / L[1]
kz = np.fft.rfftfreq(nz) * nz / L[2]

# physical limits to the wavenumbers
kmin = np.min(1.0 / L)
kmax = np.min(0.5 * dims/ L)

kbins = np.arange(kmin, kmax, kmin)
N = len(kbins)

# bin the Fourier KE into radial kbins
kx3d, ky3d, kz3d = np.meshgrid(kx, ky, kz, indexing="ij")
k = np.sqrt(kx3d ** 2 + ky3d ** 2 + kz3d ** 2)

whichbin = np.digitize(k.flat, kbins)
ncount = np.bincount(whichbin)

E_spectrum = np.zeros(len(ncount) - 1)

for n in range(1, len(ncount)):
    E_spectrum[n - 1] = np.sum(Kk.flat[whichbin == n])

k = 0.5 * (kbins[0 : N - 1] + kbins[1:N])
E_spectrum = E_spectrum[1:N]

index = np.argmax(E_spectrum)
kmax = k[index]

print(E_spectrum)

```

```

print(k)

def fft_comp(ds, irho, nindex_rho, level, low, delta, i):

    cube = ds.covering_grid(level, left_edge=low, dims=delta)

    rho = cube['density'].d

    mean_rho = np.mean(rho)
    Drho = rho - mean_rho
    Drho = Drho / mean_rho

    u = Drho[i]

    nx, ny, nz = rho.shape

    # do the FFTs -- note that since our data is real, there will be too much
    # information here. fftn puts the positive freq terms in the first half of
    # the axes -- that's what we keep. Our normalization has an '8' to account
    # for this clipping to one octant.
    ru = np.fft.fftn(rho ** nindex_rho * u)[0 : nx // 2 + 1, 0 : ny // 2 + 1, 0
        : nz // 2 + 1]
    ru = ru / (nx * ny * nz)

    return np.abs(ru) ** 2

```

Calling this function will print out two arrays, one for the k values and the other for the power spectra, that can be directly used in plotting the data in the earlier plots.

Eidesstattliche Erklärung

Ich versichere, dass ich die beigefügte schriftliche Masterarbeit selbstständig angefertigt und keine anderen als die angegebenen Hilfsmittel benutzt habe. Alle Stellen, die dem Wortlaut oder dem Sinn nach anderen Werken entnommen sind, habe ich in jedem einzelnen Fall unter genauer Angabe der Quelle deutlich als Entlehnung kenntlich gemacht. Dies gilt auch für alle Informationen, die dem Internet oder anderer elektronischer Datensammlungen entnommen wurden. Ich erkläre ferner, dass die von mir angefertigte Masterarbeit in gleicher oder ähnlicher Fassung noch nicht Bestandteil einer Studien oder Prüfungsleistung im Rahmen meines Studiums war. Die von mir eingereichte schriftliche Fassung entspricht jener auf dem elektronischen Speichermedium.

Ich bin damit einverstanden, dass die Masterarbeit veröffentlicht wird.

Hamburg, den 19/07/2021 Unterschrift: 